


# Stellar ages, masses, extinctions, and orbital parameters based on spectroscopic parameters of *Gaia* DR3<sup>★,★★</sup>

G. Kordopatis<sup>1</sup> , M. Schultheis<sup>1</sup>, P. J. McMillan<sup>2</sup>, P. A. Palicio<sup>1</sup>, P. de Laverny<sup>1</sup>, A. Recio-Blanco<sup>1</sup>, O. Creevey<sup>1</sup>, M. A. Álvarez<sup>3</sup>, R. Andrae<sup>4</sup>, E. Poggio<sup>1,5</sup>, E. Spitoni<sup>1,6</sup>, G. Contursi<sup>1</sup>, H. Zhao<sup>1</sup>, I. Oreshina-Slezak<sup>1</sup>, C. Ordenovic<sup>1</sup>, and A. Bijaoui<sup>1</sup>

<sup>1</sup> Université Côte d’Azur, Observatoire de la Côte d’Azur, CNRS, Laboratoire Lagrange, 06000 Nice, France  
e-mail: [georges.kordopatis@oca.eu](mailto:georges.kordopatis@oca.eu)

<sup>2</sup> Lund Observatory, Lund University, Department of Astronomy and Theoretical Physics, Box 43, 22100 Lund, Sweden

<sup>3</sup> CIGUS CITIC – Department of Computer Science and Information Technologies, University of A Coruña, Campus de Elviña s/n, A Coruña 15071, Spain

<sup>4</sup> Max Planck Institute for Astronomy, Königstuhl 17, 69117 Heidelberg, Germany

<sup>5</sup> Osservatorio Astrofisico di Torino, Istituto Nazionale di Astrofisica (INAF), 10025 Pino Torinese, Italy

<sup>6</sup> Stellar Astrophysics Centre, Department of Physics and Astronomy, Aarhus University, Ny Munkegade 120, 8000 Aarhus C, Denmark

Received 16 June 2022 / Accepted 13 October 2022

## ABSTRACT

**Context.** *Gaia*’s third data release provides radial velocities for 33 million stars and spectroscopically derived atmospheric parameters for more than 5 million targets. When combined with the astrometric data, these allow us to derive orbital and stellar parameters that are key to understanding the stellar populations of the Milky Way and to perform Galactic archaeology.

**Aims.** We used the calibrated atmospheric parameters, 2MASS and *Gaia*-EDR3 photometry, and parallax-based distances to compute the ages, initial stellar masses, and reddenings for the stars with spectroscopic parameters. We also derived the orbits for all of the stars with measured radial velocities and astrometry, adopting two sets of line-of-sight distances from the literature.

**Methods.** Four different sets of ages, masses, and absolute magnitudes in different photometric bands are obtained through an isochrone fitting method, considering different combinations of input parameters. The reddenings are obtained by comparing the observed colours with those obtained from the isochrone projection. Finally, the orbits are computed adopting an axisymmetric potential of the Galaxy.

**Results.** Comparisons with reference catalogues of field and cluster stars suggest that reliable ages are obtained for stars younger than 9–10 Gyr when the estimated relative age uncertainty is <50 per cent. For older stars, ages tend to be underestimated. The most reliable stellar type for age determination are turn-off stars, even when the input atmospheric parameters have large uncertainties. Ages for giants and main-sequence stars are retrieved with uncertainties of the order of 2 Gyr when extinction towards the star’s line of sight is less than  $A_V \lesssim 2.5$  mag.

**Conclusions.** The catalogue of ages, initial stellar masses, reddenings, galactocentric positions and velocities, as well as the stellar orbital actions, eccentricities, apocentre, pericentre and maximum distance from the Galactic plane reached during their orbits, is made publicly available to be downloaded. With this catalogue, the full chemo-dynamical properties of the extended solar neighbourhood unfold and allow us to better identify the properties of the spiral arms, to parametrise the dynamical heating of the disc, and to thoroughly study the chemical enrichment of the Milky Way.

**Key words.** Galaxy: kinematics and dynamics – Galaxy: stellar content – stars: fundamental parameters

## 1. Introduction

Galactic archaeology relies on the fact that stellar fossil records (chemical abundances and orbital properties) can be used to rewind time and unravel the history of the Milky Way (Freeman & Bland-Hawthorn 2002). However, in order to put the past events of our Galaxy into perspective, we also need to have access to the stellar ages, which are intrinsically difficult

to obtain for a large number of field stars (Soderblom 2010, and references therein). Asteroseismology, which is the analysis of the oscillating frequencies of stars, offers one of the most precise ways to determine stellar ages; however, it is limited to relatively bright (and nearby) targets (e.g. Miglio et al. 2013; Pinsonneault et al. 2018; Stello et al. 2022). When no asteroseismic information is available, precise and accurate atmospheric parameters (effective temperature,  $T_{\text{eff}}$ ; surface gravity,  $\log g$ ; overall metallicity,  $[M/H]$ ) and/or de-reddened colours and magnitudes are required in order to find the best fitting model from a set of theoretical isochrones. This tabulated synthetic star will hence allow us to derive the set of parameters that are not direct observables, such as the age, the mass, and the absolute magnitudes in different photometric bands. This technique is called the isochrone projection method (e.g. Jørgensen & Lindegren 2005).

\* Full Table A.1 is only available at the CDS via anonymous ftp to [cdsarc.cds.unistra.fr](https://cdsarc.cds.unistra.fr) (130.79.128.5) or via <https://cdsarc.cds.unistra.fr/viz-bin/cat/J/A+A/669/A104>

\*\* The parameters computed in this paper have been prepared in the context of *Gaia*’s Performance verification paper concerning the Chemical cartography of the Milky Way (Gaia Collaboration 2023a).

The advent of large stellar spectroscopic surveys more than 15 yr ago saw the development of the first isochrone projection codes, which had the main goal of deriving the line-of-sight distances via the distance modulus and the (projected) absolute magnitudes. Although these methods naturally delivered the stellar ages as an output (e.g. Zwitter et al. 2010; Binney et al. 2014), the uncertainties that were associated with them were beyond the acceptable for Galactic archaeology, unless stellar distance was known in order to constrain the projection (e.g. Kordopatis et al. 2016, for an application with stars in the Carina dwarf spheroidal galaxy).

Data gathered by the European Space Agency satellite *Gaia* (Gaia Collaboration 2016a,b, 2018a, 2021a, 2023c) has undoubtedly opened a new era regarding the age determination. Stellar parallaxes ( $\varpi$ ), and heliocentric line-of-sight distances derived from them (e.g. Bailer-Jones 2015; Luri et al. 2018; Schönrich et al. 2019; Anders et al. 2019), can now be used in the projection, in combination with the precise photometry ( $G$ ,  $G_{BP}$ ,  $G_{RP}$ ), reducing significantly the age uncertainties (e.g. McMillan et al. 2018; Sanders & Das 2018; Queiroz et al. 2018; Leung & Bovy 2019; Feuillet et al. 2019).

Within *Gaia*'s Data Processing Analysis Consortium (DPAC), the Astrophysical parameters inference system (Apsis; Bailer-Jones et al. 2013; Creevey et al. 2023; Fouesneau et al. 2023; Delchambre et al. 2023) is the work chain in charge of obtaining the physical parameters<sup>1</sup> of the targets observed by the satellite. More specifically, the stellar parameters for single stars are obtained from six different modules, reflecting either the different nature of the input data taken into account by each of them and/or the different stellar types they deal with. Amongst these modules, the General Stellar Parametrizer from Photometry (GSP-Phot), the General Stellar Parametrizer from Spectroscopy (GSP-Spec), and the Final Luminosity Age Mass Estimator (FLAME) are the ones deriving parameters for most of the targets.

On the one hand, GSP-Phot obtained the  $T_{\text{eff}}$ ,  $\log g$ ,  $[M/H]$ , absolute magnitude in the  $G$  band, radius, extinction, and line-of-sight distance of  $\sim 400$  million stars of OBAFGKM spectral-type, based on the analysis of the very low-resolution Blue and Red Spectrophotometers (120 flux points, each, with a resolving power ranging from 20 to 90 depending on the wavelength), in combination with the parallaxes. Overall, the parameters show a median absolute deviation (MAD) compared to the literature of  $\sim 220$  K, 0.25 dex, and 0.26 dex for  $T_{\text{eff}}$ ,  $\log g$ , and  $[M/H]$ , respectively. There are limitations, however, depending on the stellar type, the metallicity regime, and the true extinction along the line of sight, due to the low resolution of the input data, and to the degeneracy between  $T_{\text{eff}}$  and extinction (Andrae et al. 2018, 2023).

On the other hand, GSP-Spec avoids the limitations of GSP-Phot by analysing the medium-resolution spectra ( $R = \lambda/\delta\lambda \approx 11\,000$ ) gathered by the Radial Velocity Spectrometer (RVS). However, only the targets whose spectra have an adequate signal-to-noise ratio ( $S/N > 20$ ) have published parameters, which represents only a fraction of stars ( $\sim 5 \times 10^6$  targets of FGK stellar-type, Recio-Blanco et al. 2023). The stated MAD compared to the literature values for  $T_{\text{eff}}$ ,  $\log g$ , and  $[M/H]$  are 61 K, 0.14 dex, and 0.09 dex, whereas  $\alpha$ -element enhancement ( $[\alpha/Fe]$ ) and a handful of elemental abundances are also provided for a subsample.

Finally, the FLAME module derived two sets of masses ( $M$ ), ages ( $\tau$ ), and evolutionary phases for most *Gaia* sources,

based on either GSP-Phot or GSP-Spec results. These evolutionary parameters were obtained by first computing a bolometric correction for each target (based on the effective temperature, surface gravity, and metallicity), then deriving the bolometric luminosity  $\mathcal{L}$  (via the relation linking  $\mathcal{L}$  with the absolute magnitude of the star), and finally getting the stellar radius  $\mathcal{R}$  via the Stefan-Boltzmann relation linking  $\mathcal{R}$  with  $\mathcal{L}$ . The luminosities and radii are then projected on BaSTI (Hidalgo et al. 2018) isochrones of solar metallicity to obtain  $\tau$  and  $M$ .

In this paper we build upon the *Gaia* public catalogues, and focus on the RVS sample of GDR3. This sample contains  $\sim 33 \times 10^6$  stars with radial velocity measurements and  $5 \times 10^6$  stars with spectroscopic parameters and abundances (Recio-Blanco et al. 2023; Fouesneau et al. 2023). We performed an improved projection on the isochrones that takes into account the necessary GSP-Spec calibrations of metallicity and surface gravities<sup>2</sup>, stellar distance (in a different way to FLAME, using the Bailer-Jones et al. 2021 values), infrared (2MASS, Skrutskie et al. 2006), and EDR3 photometry. Furthermore, for the community's convenience, we also computed and provide the catalogue of the three-dimensional galactocentric positions, (cylindrical) velocities, and orbital parameters of all of the GDR3 RVS stars using an updated version of the axisymmetric Galactic potential of McMillan (2017) and the Galpy code (Bovy 2015).

Section 2 describes the way the ages, the masses, the absolute magnitudes, and the reddenings were computed. In particular, this section contains a description of the isochrone sets that we adopted, and the validation of the projected parameters. Section 3 discusses how the orbital parameters were obtained, and illustrates how the ages and masses correlate with them. We present our conclusions in Sect. 4. The catalogue containing all of these parameters can be downloaded from CDS, and in *hdF* format at the link indicated in the footnote<sup>3</sup>; the different columns are described in Table A.1.

## 2. Catalogue of ages, initial stellar masses, extinctions, and reddenings

This section describes the sets of isochrones we employ in this work (Sect. 2.1). The mathematical basis of the algorithm is presented in Sect. 2.2, and the priors that are used to optimise the isochrone projection are justified in Sect. 2.3. The method's accuracy and precision are tested on synthetic data extracted from isochrones in Sect. 2.4. Points to consider when projecting real data, such as colour- $T_{\text{eff}}$  calibration or the effect of  $\alpha$ -enhancement on the overall metallicity, are discussed in Sect. 2.5. The actual projection of the calibrated GSP-Spec parameters is done in Sect. 2.6. The compiled age and mass sample is compared and validated with respect to reference catalogue of field and cluster stars in Sect. 2.7. Finally, reddenings and absolute magnitudes derived from the projection are discussed in Sects. 2.8 and 2.9.

### 2.1. Definition of the isochrone set

We used the PARSEC stellar tracks (Bressan et al. 2012) version 1.2S (Tang et al. 2014; Chen et al. 2015) up to the beginning of asymptotic giant branch (AGB), and the COLIBRI  $S_{37}$

<sup>2</sup> Due to the tight schedule of DPAC to publish GDR3, FLAME parameters based on GSP-Spec's parameters did not use the calibrated values, as the latter came after the computation of parameters from the former.

<sup>3</sup> <https://ftp.oca.eu/pub/gkordo/GDR3/>

<sup>1</sup> As opposed to the astrometric parameters.

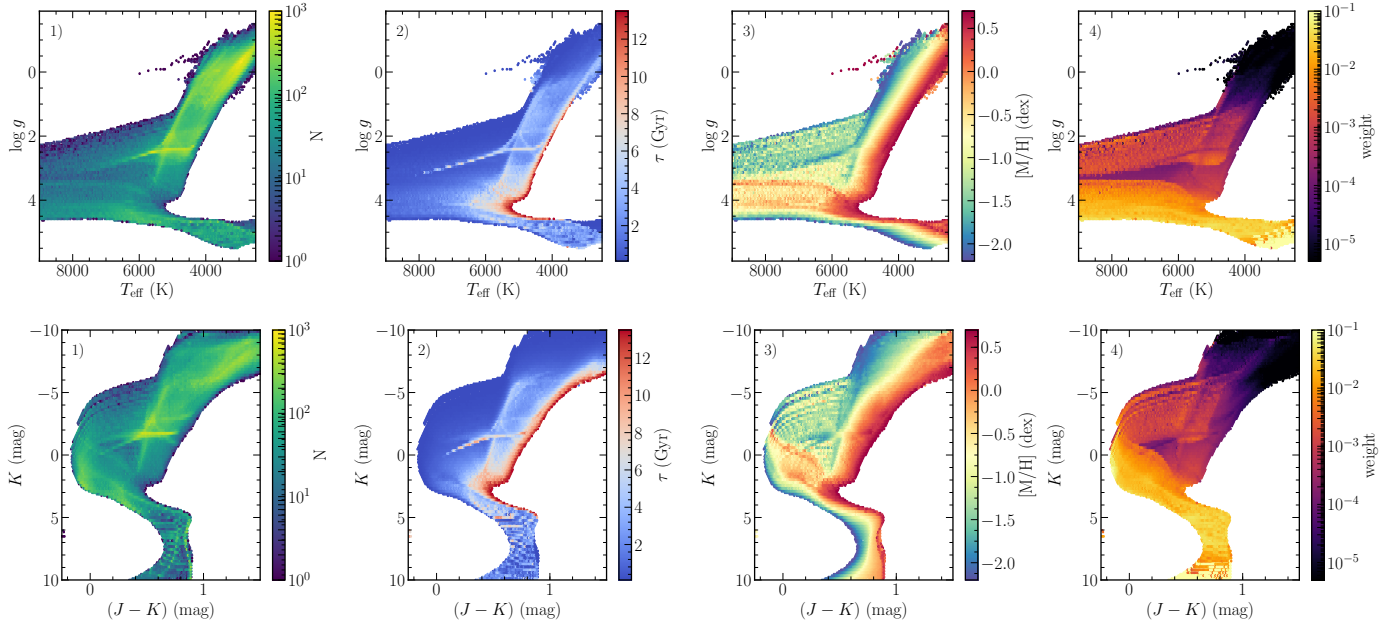


**Fig. 1.**  $T_{\text{eff}}$  vs.  $\log g$  (top) and  $(J - K_s)$  vs.  $K_s$  (bottom) hexbin plots of the isochrones employed in this work to derive the ages, masses, and reddenings. *Panels 1:* are colour-coded by density of points, *Panels 2:* by average age, *Panels 3:* by average metallicity, and *Panels 4:* by average evolutionary weight (factor  $\beta_i$  in Eq. (1)).

tracks up to the end of the AGB phase (Pastorelli et al. 2020; Marigo et al. 2013; Rosenfield et al. 2016), in combination with the online interpolator tool<sup>4</sup> of the Padova group, to compute a library of isochrones spanning ages between 0.1 and 13.5 Gyr logarithmically spaced by a  $\log(\tau)$  step of 0.05, and the metallicities between  $-2.2$  and  $+0.7$  dex with a step of 0.05 dex (i.e. of the same order as the GSP-Spec uncertainties on metallicity). The metallicity values for the isochrones were obtained using the approximation  $[M/H] = \log(Z/X) - \log(Z/X)_\odot$ , with  $(Z/X)_\odot = 0.0207$  and  $Y = 0.2485 + 1.78Z$ , and where  $X, Y, Z$  are respectively the hydrogen, helium, and metal abundances by mass (Caffau et al. 2011; Basu & Antia 1997).

In total, 2301 different isochrone tracks, containing 842 494 tabulated  $T_{\text{eff}}$ ,  $\log g$ ,  $[M/H]$ ,  $\tau$ , initial stellar mass ( $M_{\text{ini}}$ ), absolute magnitudes in the  $G, G_{BP}, G_{RP}$  EGDR3 photometric bands and in the 2MASS  $J, H, K_s$  bands were obtained in this way. Their  $T_{\text{eff}}$  versus  $\log g$  and  $(J - K_s)$  versus  $K_s$  distribution and properties are shown in Fig. 1. This set of isochrones is used in what follows to project the atmospheric parameters on.

## 2.2. Isochrone projection algorithm

The method described below was initially inspired by Zwitter et al. (2010) and early implementations of it have already been successfully employed for either distance computation (Kordopatis et al. 2011, 2013, 2015b; Recio-Blanco et al. 2014), age derivation (Kordopatis et al. 2016; Magrini et al. 2017, 2018; Santos-Peral et al. 2021), or reddening estimation (Schultheis et al. 2015; Zhao et al. 2021). For completeness, we summarise in what follows the method, which contains the specific changes implemented for the *Gaia*-RVs application.

We consider a star in the *Gaia* catalogue that is associated with a set of observed parameters  $\hat{\theta}_k$  ( $k \equiv T_{\text{eff}}, \log g, [M/H], G, J, H, K_s, \dots$ ) and uncertainties  $\sigma_{\hat{\theta}_k}$ . The projection on the isochrones is performed as follows.

In step 1 we select all of the isochrone points that have tabulated values within  $n \cdot \sigma_{\hat{\theta}_k}$  from each considered observed parameter, where  $n$  is arbitrarily chosen by the user. If fewer than 50 points are selected, the range is expanded to  $3n \cdot \sigma_{\hat{\theta}_k}$ . This usually happens when the observed uncertainties are largely underestimated.

In step 2, we assign for each selected node on the isochrones a Gaussian weight,  $w_i$ , that depends primarily on its distance from the measured observables. In practice,

$$w_i = p_i \cdot \beta_i \cdot \exp\left(-\sum_k \frac{(\theta_{i,k} - \hat{\theta}_k)^2}{2\sigma_{\hat{\theta}_k}^2}\right), \quad (1)$$

where  $\theta_{i,k}$  corresponds to the tabulated parameters of the isochrones. The factor  $\beta_i$ , suggested by Zwitter et al. (2010), is defined as the stellar mass difference between two adjacent points on the same isochrone. It is equivalent to assuming a flat prior on stellar mass and provides a higher probability of observing dwarfs, reflecting their slower evolutionary phases (see panel 4 of Fig. 1). The parameter  $p_i$  is the prior on the age. It is equal to one if a flat prior is considered, or it can be a more complex function depending on the a priori knowledge of the investigated stellar population. The prior adopted in this work is shown in Fig. 2, and is discussed in Sect. 2.3.

In step 3 the projected parameters,  $\theta_k^*$ , are obtained by computing the weighted mean of the selected set of tabulated stars with parameters  $\theta_k$ :

$$\theta_k^* = \frac{\sum_i w_i \cdot \theta_{k,i}}{\sum_i w_i}. \quad (2)$$

Finally, the associated uncertainty is obtained by computing the weighted dispersion:

$$\sigma_{\theta_k^*} = \sqrt{\frac{\sum_i w_i \cdot (\theta_k^* - \theta_{k,i})^2}{\sum_i w_i}}. \quad (3)$$

Because in practice the method computes as many weights  $w_i$  as points on the isochrones, restricting the computation to

<sup>4</sup> Version 3.5, [http://stev.oapd.inaf.it/cgi-bin/cmd\\_3.5](http://stev.oapd.inaf.it/cgi-bin/cmd_3.5)

the points within  $4 \cdot \sigma_{\hat{\theta}_k}$  from the measurements (step 1, above) ensures a significant speed-up of the algorithm without losing any contribution from isochrone points that are far from the input data. In addition, step 1 also ensures that no age or mass is returned if the measured parameters are too far from the set of isochrones. This is particularly crucial for the very low-metallicity stars ( $[M/H] < -2.2$  dex) since, in principle, a  $T_{\text{eff}} - \log g$  match could be found, despite being far from the edge of the grid of isochrones.

Eventually, the algorithm returns as many parameters as are tabulated on the isochrones. However, we store only the projected  $T_{\text{eff}}$ ;  $\log g$  and  $[M/H]$ ; the age ( $\tau$ ); the initial stellar mass ( $M_{\text{ini}}$ ); and the absolute magnitudes  $G$ ,  $G_{BP}$ ,  $G_{RP}$ , and their associated uncertainties. From the projected magnitudes, we can also infer the interstellar reddening,  $E(G_{BP} - G_{RP})$ , and the interstellar extinction,  $A_G$  (see Sect. 2.8).

We note that the difference between the input  $T_{\text{eff}}$ ,  $\log g$  and  $[M/H]$ , and the output (i.e. projected) values can serve as diagnostics of the projection. Typically, when the difference is too large<sup>5</sup>, this implies that no isochrones are found nearby the input values, therefore calling into question the reliability of the output parameters (and perhaps the input ones as well).

### 2.3. Choice of an age prior

Unlike some isochrone projection methods available in the literature (some of them optimised to only get the line-of-sight distances, see Sect. 1), the one we present in this paper does not adopt a specific age prior based on Galactic populations (see Fig. 2). For the majority of the stars ( $-0.7 \leq [M/H] \leq 0$  dex) a flat prior is adopted. This choice is motivated by the facts that the definitions of thin and thick discs are not as clear as they used to be (chemical vs. geometrical discs; see e.g. Hayden et al. 2017), that the *Gaia*-Enceladus-Sausage spatial and chemical distribution is complex and partly entangled with the disc (see e.g. Belokurov et al. 2018; Helmi et al. 2018; Myeong et al. 2019; Feuillet et al. 2020), and that the properties of many of the other accreted populations highlighted with *Gaia* show that a given locus in physical and chemical spaces is a mix of several different populations of different ages (e.g. Kordopatis et al. 2020; Laporte et al. 2020; Naidu et al. 2020; Gaia Collaboration 2021a, and references therein).

Such a flat age prior, however, is poorly justified for super-solar metallicity or metal-poor stars, for which we can safely suppose that the former cannot be too old (metal-rich bulge stars are  $\sim 9$  Gyr, e.g. Schultheis et al. 2017; Bovy et al. 2019) and that the latter cannot be too young (the most metal-poor thin-disc stars in the solar neighbourhood are found to be  $\sim 8-9$  Gyr old, whereas the thick disc is found to be older than  $7-8$  Gyr, see e.g. Bensby et al. 2014; Haywood et al. 2018). For this reason we adopt half-Gaussian weights, for  $\tau > \tau_c$  if  $[M/H] > 0$  or  $\tau < \tau_c$  if  $[M/H] < -0.7$  dex:

$$p = \exp\left(-\frac{(\tau - \tau_c)^2}{2 \cdot \sigma_\tau^2}\right). \quad (4)$$

We take  $\tau_c = 10$  Gyr for  $[M/H] > 0$  dex and  $[M/H] < -2$  dex, meaning that a star has less probability of being older than 10 Gyr if it has a super-solar metallicity and less probability of

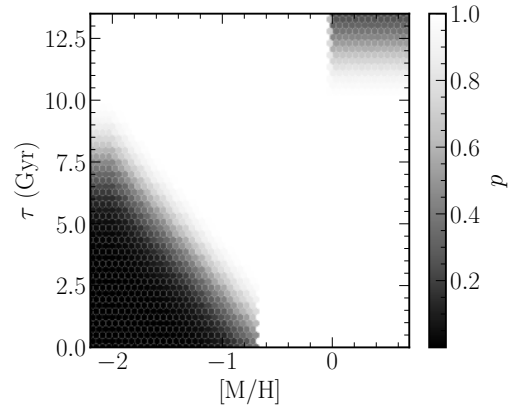


**Fig. 2.** Age priors,  $p$ , adopted in this work, used in Eq. (1). These are half-Gaussians of  $\sigma = 2$  Gyr, centred on different ages depending on the metallicity.

**Table 1.** Uncertainty percentiles for the GSP-Spec sample adopted for the performance tests of the projection method.

Parameter	Q25	Q50	Q75	Q95
$T_{\text{eff}}$ (K)	35	70	130	350
$\log g$ ( $g$ in $\text{cm s}^{-2}$ )	0.1	0.2	0.35	0.5
$[M/H]$ (dex)	0.05	0.1	0.2	0.4
$G$ (mag)	0.015	0.03	0.06	0.14
$J, H, K_s$ (mag)	0.03	0.04	0.07	0.15

being younger than 10 Gyr if it is more metal-poor than  $-2$  dex. For stars with  $-2 < [M/H] < -0.7$  dex, we adopt

$$\tau_c = -5.4 \cdot [M/H] - 0.8, \quad (5)$$

which imposes  $\tau_c = 3$  Gyr at  $[M/H] = -0.7$  dex and  $\tau_c = 10$  Gyr at  $[M/H] = -2$  dex. The resulting weights as a function of metallicity are shown in Fig. 2.

### 2.4. Validation of the method on synthetic data

In order to evaluate the method's performance, we first test it on a set of synthetic data. We randomly select, amongst the entire isochrone set (Sect. 2.1), 200 turn-off stars (defined as  $5000 \leq T_{\text{eff}} \leq 8500$  K and  $\log g \geq 3.5$ ), 200 red giant branch (RGB) stars (defined as  $T_{\text{eff}} \leq 6000$  K and  $\log g < 3.5$ ), and 200 main-sequence stars (defined as  $T_{\text{eff}} < 4800$  K and  $\log g \geq 4.0$ ). We note that this sample contains non-realistic stars (e.g. metal-rich stars older than 12 Gyr). We make sure, however, not to select stars younger than 5 Gyr with metallicities lower than  $-1$  dex.

We consider four different types of projection, labelled as follows:

- spec: projects only  $\hat{\theta}_k = \{T_{\text{eff}}, \log g, [M/H]\}$ .
- speck: projects  $\{T_{\text{eff}}, \log g, [M/H], K_s\}$ .
- specjhk: projects  $\{T_{\text{eff}}, \log g, [M/H], J, H, K_s\}$ .
- specjhkg: projects  $\{T_{\text{eff}}, \log g, [M/H], J, H, K_s, G\}$ .

In addition, we consider different test cases, where the value of each of the input parameters is randomised according to a normal distribution of standard deviation associated with a given uncertainty (see Table 1). The sample labelled ‘Q25’ adopts the parameter uncertainties of the 25th percentile of the GSP-Spec catalogue for a given specific parameter. Similarly, Q50 and Q95 adopt the uncertainties of the 50th and 95th percentiles.

<sup>5</sup> Empirically, when dealing with real *Gaia* data, we have found that thresholds of 200 K in  $T_{\text{eff}}$ , 0.3 dex in  $\log g$ , and 0.1 dex in  $[M/H]$  are enough to remove outliers. Other values, though, may be selected by the users depending on the application.

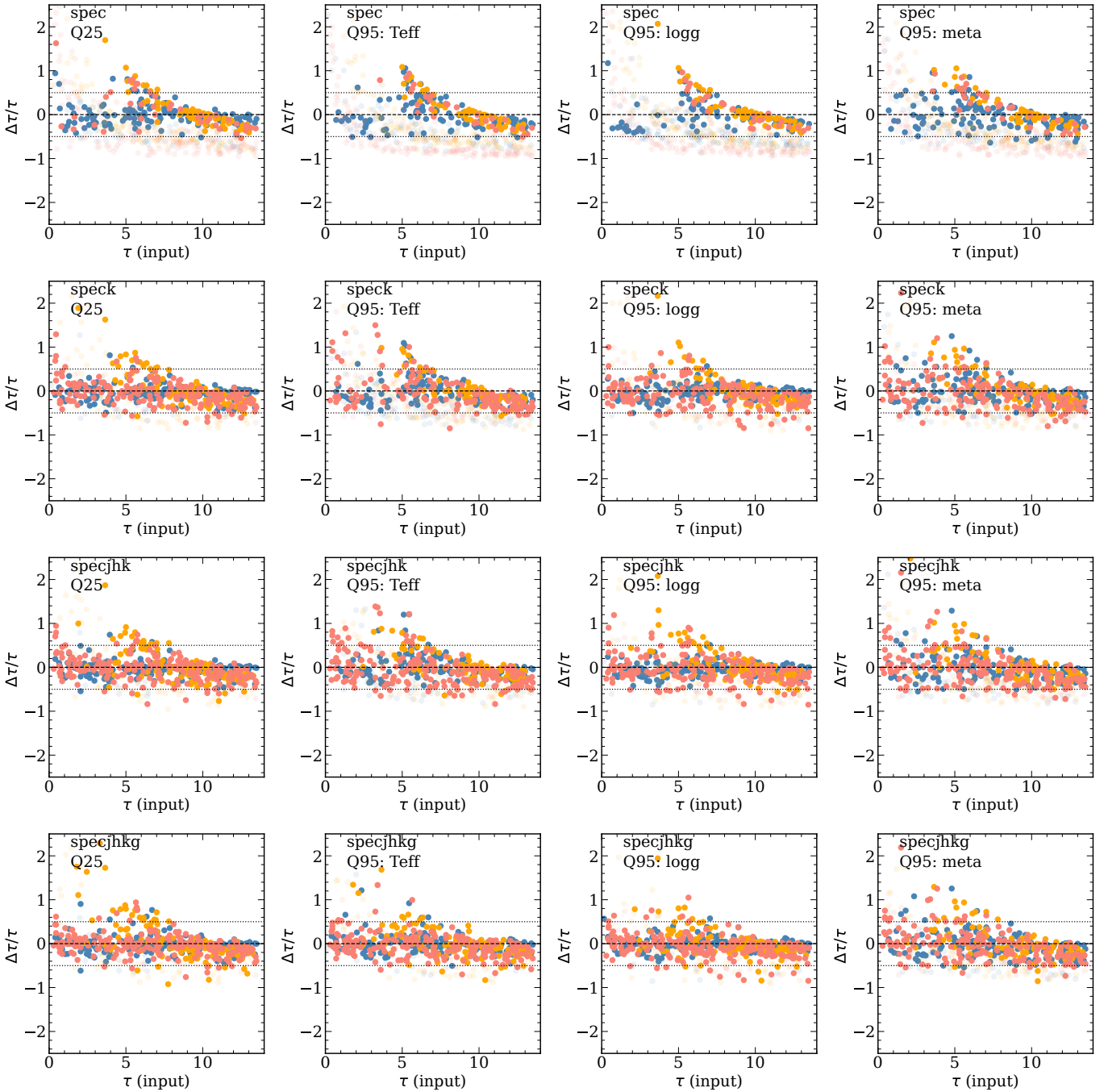


**Fig. 3.** True vs. relative age error (i.e. (output-input)/input) for the test sample of synthetic data. The blue, orange, and red points represent turn-off, main-sequence, and red giant stars, respectively. The dashed black line represents the 1:1 relation, where a star with a perfectly well estimated age should lie. The dotted lines show deviations from perfect estimation of  $\pm 50$  per cent. Input parameters are randomised according to the Q25 uncertainties (see Table 1) unless specified in the top left corner. The first row plots consider a projection of only  $T_{\text{eff}}$ ,  $\log g$ , and  $[M/H]$  (labelled *spec*), whereas rows two to four also consider the  $K_s$  magnitude (*speck*); the  $J, H, K_s$  magnitudes (*specjhk*); and the  $J, H, K_s, G$  magnitudes (*specjhkg*), respectively. Finally, solid points are the stars for which the estimated relative age uncertainty is smaller than 50 per cent, whereas the semi-transparent points have estimated relative age uncertainties larger than 50 per cent. See Sect. 2.4 for further details.

We note that the uncertainties for the photometric filters are estimated as the quadratic sum of the uncertainty of the apparent magnitude in that filter and the uncertainty on the absolute magnitude derived by the distance modulus<sup>6</sup> (see Sect. 2.6.1 for further details).

<sup>6</sup> Main-sequence stars with large uncertainties on their atmospheric parameters usually have small uncertainties on their distance modulus as they are relatively nearby.

Figures 3 and 4 compare the real ages and masses with their relative errors, where each row shows a different projection flavour. Q25 uncertainties are adopted for all of the parameters, except for columns two to four, where one parameter each time adopts Q95, as indicated at the top left corner (while keeping the other parameters at Q25). These figures show that, provided we apply a 50 per cent filter on the estimated relative age uncertainty, the ages for turn-off stars are almost always well determined, even when input parameter uncertainties are large (Q95).

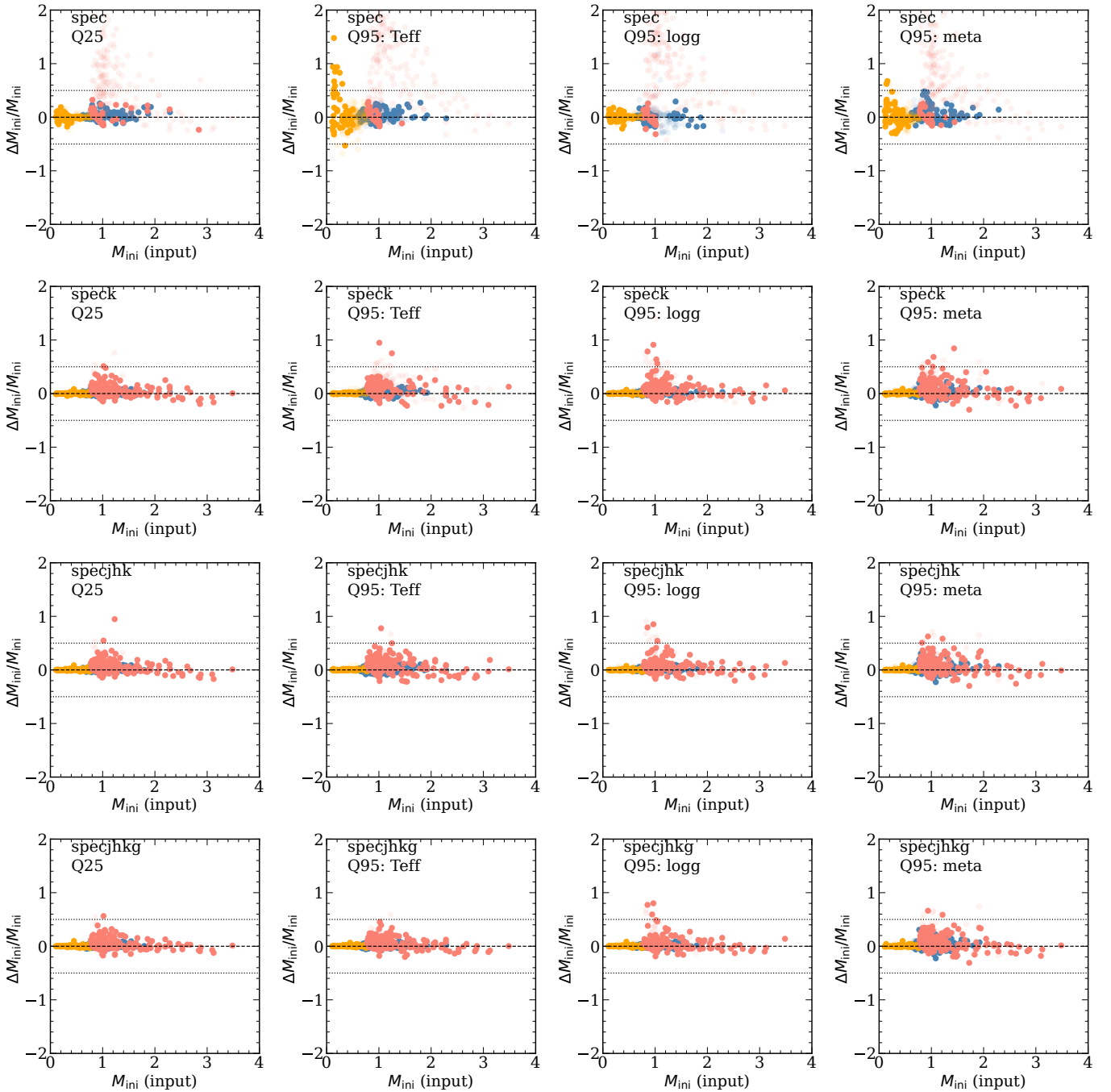


**Fig. 4.** Same as Fig. 3, but for initial stellar masses. The semi-transparent points are stars with estimated relative age uncertainties greater than 50 per cent, whereas the filled circles are stars with estimated age uncertainties smaller than 50 per cent.

On the other hand, giants and main-sequence stars require additional information to be used during the projection (which can be in the form of absolute magnitudes or age priors) in order to have their ages well derived. When this is done, *speck*, *specjhk*, and *specjhkg* return reliable estimations (age errors smaller than 50 per cent) for all of the stellar types, even with Q95 input uncertainties.

The mass estimations for main-sequence and turn-off stars are always reliable<sup>7</sup>, regardless of the projection flavour or input parameter uncertainties. This is not the case for giants where

<sup>7</sup> Unless for masses smaller than  $0.3 M_{\odot}$  when the  $T_{\text{eff}}$  uncertainty is Q95.

the *spec* projection overestimates the values. Furthermore, we find that the mass uncertainties are generally underestimated, and that a filtering on the age uncertainty removes the outliers more efficiently, at the cost of removing simultaneously the mass estimations for the main-sequence stars. In what follows we filter-out the masses solely of the giants, but only if their relative age uncertainty is larger than 50 per cent.

Finally, we also investigated the effect of magnitude uncertainties, as well as interstellar reddening on the output parameters. For this test-case we set uncertainties for  $T_{\text{eff}}$ ,  $\log g$ , and  $[M/H]$  always equal to Q50, whereas we adopted uncertainties for  $J$ ,  $H$ ,  $K_s$ , and  $G$  of Q25 and Q95. Three different extinction values were considered:  $A_V = 0.0$  mag,  $A_V = 0.2$  mag, and

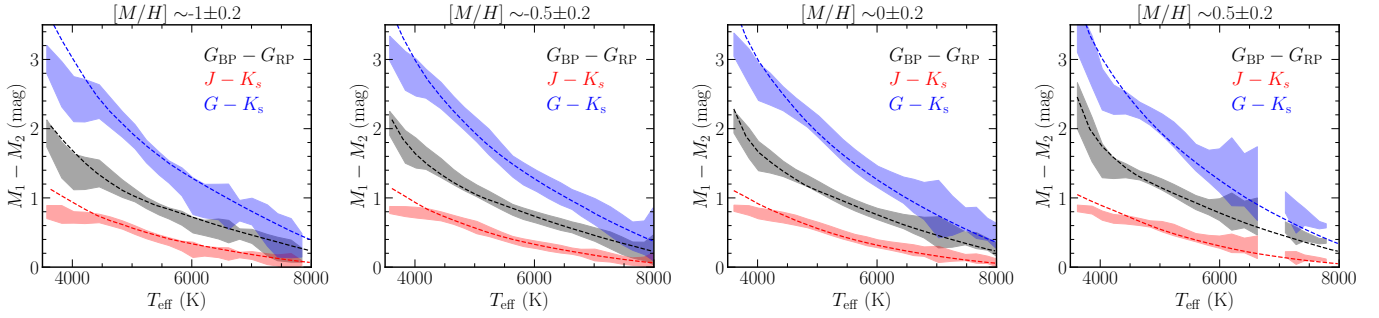


**Fig. 5.** Relation between  $T_{\text{eff}}$  and  $G_{BP} - G_{RP}$  (black),  $J - K_s$  (red),  $G - K_s$  (blue) for the adopted isochrones (in dashed lines), and the relations obtained from *Gaia*-RVS observed stars (coloured surfaces representing the  $1\sigma$  dispersion) within 150 pc from the Sun (to minimise the extinction effects) at four different metallicity regimes.

$A_V = 2.5$  mag (converted for each filter; see Sect. 2.6.2). Results for the ages are shown in Appendix B. In short, the speck projection always gives good ages and masses, even with Q95 and  $A_V = 2.5$  mag. We find that  $A_V = 0.3$  introduces small biases for specjhk and specjhkg if the uncertainties on the magnitudes are small (i.e. Q25), but this bias mostly disappears for larger uncertainties (Q95).

### 2.5. Specific considerations for projection of real data

When projecting real *Gaia* data on the isochrones, some specific points that were not considered in the previous sections need to be taken into account: the colour-calibration of the isochrones, the  $\alpha$ -enhancement of the stars, and the choice of the isochrone libraries. We discuss these points below.

#### 2.5.1. Colour- $T_{\text{eff}}$ calibration

For a reliable projection on the isochrones (or if the output  $G_{BP}$  and  $G_{RP}$  magnitudes is wanted; see Sect. 2.8), the relation between the  $T_{\text{eff}}$  and the colour indexes must be the same for the observed values (in our case GSP-Spec) and for the values on the isochrones. Following Santos-Peral et al. (2021), we investigated the relation between these two, for four different metallicity regimes ( $-1, -0.5, 0, +0.5$  dex) for stars closer than 150 pc from the Sun, in order to minimise the effect of reddening on the observed colours. The results shown in Fig. 5 suggest no significant differences between the isochrone and the observed relations, at least for stars hotter than 4000 K, therefore implying that no specific calibration needs to be performed on the isochrone colours in order to be on the same scale as the GSP-Spec  $T_{\text{eff}}$ .

#### 2.5.2. Effect of non-solar $\alpha$ -enhancement

PARSEC isochrones do not include any variation of  $\alpha$ -abundance, all of the sets adopting the solar value. In order to evaluate the effect of non-solar  $\alpha$ -enhancement, we used the Salaris et al. (1993) formula, as derived in Valentini et al. (2019), to convert the GSP-Spec calibrated  $[M/H]$  to a proxy for the overall metallicity including  $\alpha$ -elements,  $[M/H]_\alpha$ . We adopted the formula

$$[M/H]_\alpha = [M/H]_{\text{GSP-Spec}} + \log_{10}(C \times 10^{[\alpha/\text{Fe}]} + (1 - C)), \quad (6)$$

with  $C = 0.661$ , and with  $[\alpha/\text{Fe}]$  the calibrated value provided by GSP-Spec obtained with a third-degree polynomial (see first row of Table 4 in Recio-Blanco et al. 2023).

Using the spec projection, adopting one or the other metallicity estimate, resulted in differences smaller than 1 Gyr and

$0.1 M_\odot$  for 90 per cent of the stars, for  $\tau$  and  $M_{\text{ini}}$ , respectively. Given that these differences are smaller than the uncertainty on the derived ages and masses, and that  $[\alpha/\text{Fe}]$  abundances have a precision of the order of  $\sim 0.07$  dex (which can become larger depending on the quality of the spectra; see Recio-Blanco et al. 2023), we decided not to use  $[M/H]_\alpha$ . However, projections obtained using  $[M/H]_\alpha$  can be provided upon request to the first author.

#### 2.5.3. Choice of isochrone libraries

The choice of an isochrone library on which to project the observed parameters, can affect the derived results. It is beyond the scope of this paper to discuss the differences, in terms of input physics or shape, between the various libraries found in the literature: Yonsei-Yale (Demarque et al. 2004), BaSTI (Hidalgo et al. 2018), MIST (Dotter 2016), and DSEP (Dotter et al. 2008), among others. However, we illustrate qualitatively in Fig. 6 how such a choice may affect the derived ages. Figure 6 compares MIST isochrones of a given age  $\tau$  and iron content  $[\text{Fe}/\text{H}]$  (indicated in the top left corner of each line) with PARSEC isochrones of equal metallicity and age (in grey),  $\tau - 20$  per cent (in blue), and  $\tau + 20$  per cent (in red). Typical Q50 uncertainties in  $T_{\text{eff}}$ ,  $\log g$ , and  $G$  for GSP-Spec stars of similar metallicity are also plotted within each panel.

Compared to PARSEC isochrones of the same age and metallicity, MIST isochrones tend to have redder RGBs, and either bluer turn-offs for metal-poor stars or redder ones for metal-rich populations, whereas good agreement exists for the solar isochrone. Overall, the differences are well within 20 per cent. This value is comparable to the age uncertainties that are derived.

### 2.6. *Gaia* DR3 application: Computation of the datasets

#### 2.6.1. Projection flavours, input parameters, and associated uncertainties

We performed four different isochrone projections (leading to four sets of ages, masses, and interstellar extinctions) according to the flavours described in Sect. 2.4: spec, speck, specjhk, and specjhkg.

The atmospheric parameters are the calibrated GSP-Spec values, following Eq. ((1) for  $\log g$ ) and Eq. ((3) for  $[M/H]$ , with a fourth-degree polynomial) of Recio-Blanco et al. (2023). The absolute magnitudes in the  $G$ ,  $J$ ,  $H$ , and  $K_s$  bands were obtained using the distance modulus, adopting the Bailer-Jones et al. (2021) geometric distances ( $r$ ) that assume a distance prior

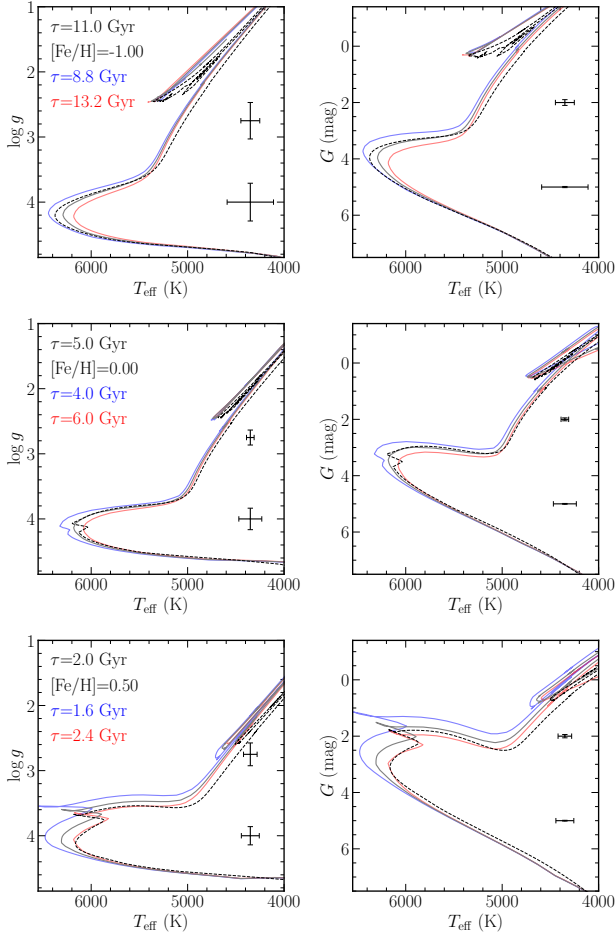


**Fig. 6.** MIST isochrones (dashed black lines) in two different spaces:  $T_{\text{eff}}$  vs.  $\log g$  (left) and  $T_{\text{eff}}$  vs.  $G$  (right), for an old metal-poor population (top), a 5 Gyr solar metallicity population (middle), and a young super-solar metallicity population (bottom). In each panel, three PARSEC isochrones with the same metallicity are plotted, one at equal age (grey solid line), one at  $\tau - 20$  per cent (blue solid line), and one at  $\tau + 20$  per cent (red solid line). Typical  $T_{\text{eff}}$ ,  $\log g$ , and  $G$  uncertainties (Q50) for giants ( $\log g < 3.5$ ) and dwarfs ( $\log g > 3.5$ ) for stars at  $[M/H] = [\text{Fe}/H] \pm 0.2$  dex are also plotted on the right side of each panel.

along with the parallax information, and neglecting entirely the line-of-sight extinction. Although this assumption has no consequence for the spec projection, neglecting the line-of-sight extinction introduces an increasing amount of bias in the output ages and masses the bluer the central wavelengths of the filter (i.e. in increasing order,  $K_s$ ,  $H$ ,  $J$ , and lastly  $G$ ; see Appendix B).

The uncertainties required in Eq. (1) for the projection were obtained assuming Gaussian posteriors for GSP-Spec  $T_{\text{eff}}$ ,  $\log g$ , and  $[M/H]$  (i.e. taking half of the difference between the upper and lower confidence value). The uncertainty on the absolute magnitudes,  $M_\lambda$ , for a given filter,  $\lambda$ , are obtained as the quadratic sum of the uncertainty on the observed magnitude,  $m_\lambda$ , and the uncertainty term coming from the distance modulus,  $\mu$ :

$$\sigma_{M_\lambda} = \sqrt{\sigma_\mu^2 + \sigma_{m_\lambda}^2}. \quad (7)$$

Here  $\sigma_\mu$  is the uncertainty on the distance modulus derived using standard error analysis

$$\sigma_\mu = \frac{\sigma_r}{0.461 \cdot r}, \quad (8)$$

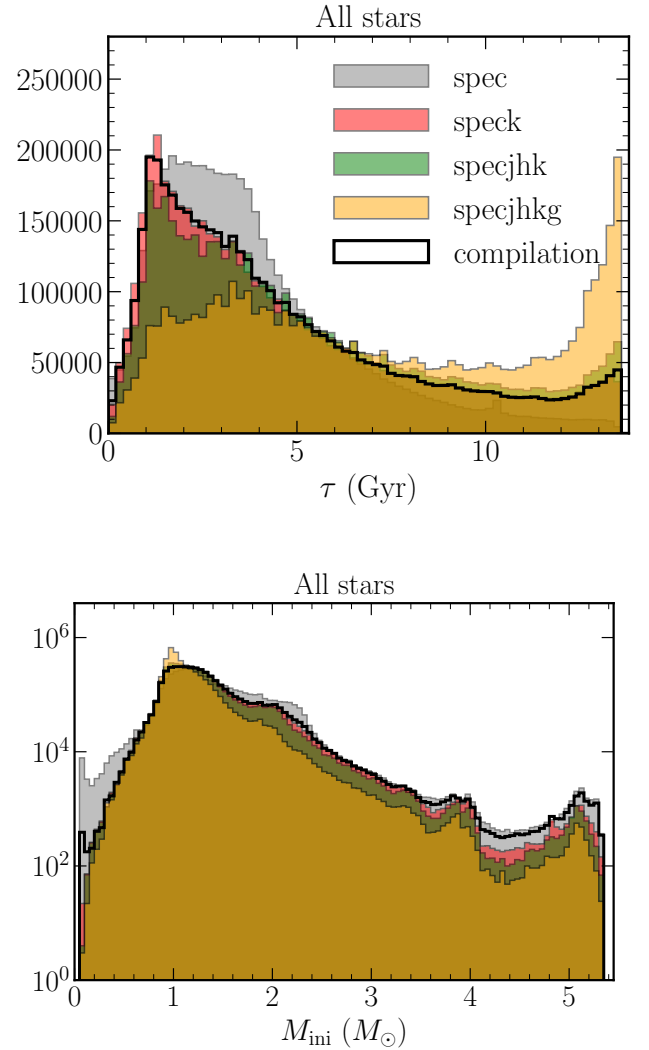


**Fig. 7.** Histograms of age (top) and initial mass (bottom, in logarithmic scale) of each projection flavour and for the compiled sample, for all the GSP-Spec stars that have a `KMgiantPar_flag = 0`.

with  $\sigma_r$  the (assumed) Gaussian uncertainty on the distance ( $r$ ), obtained also as half of the difference between the upper and the lower confidence value of  $r$ .

Figure 7 compares the age (top) and mass (bottom) distributions of the different projections. Each distribution contains all of the GSP-Spec stars, except those having `KMgiantPar_flag`  $\neq 0$ , for which  $T_{\text{eff}}$  and  $\log g$  are less reliable (see Recio-Blanco et al. 2023). One can see that the `specjhg` projection finds significantly older stars, especially compared to the `spec` projection, which shows the youngest ages, on average, with a broad peak at  $\tau \sim 3.5$  Gyr. These differences can be understood given the analyses in the previous sections; on the one hand, as extinction is not taken into account in the `speck`, `specjhk`, and `specjhkg` projections, giants with reddened colours tend to lie on older isochrones, biasing the age estimation towards larger values. As shown in Appendix B, this bias is stronger the bluer the filter, eventually leading to the peak at  $\tau \sim 12$  Gyr for the `specjhkg` projection. On the other hand, the spectroscopic projection (see Fig. 3) tends to be biased towards younger ages for all stellar types except the turn-off stars.



**Table 2.** Extinction conversions, as adopted from PARSEC 3.5.

	$A_J$	$A_H$	$A_{K_s}$	$A_G$
$A_\lambda/A_V$	0.28665	0.18082	0.11675	0.83278

## 2.6.2. Catalogue compilation

The differences seen in Fig. 7 naturally lead to the necessity of finding an optimal combination of projection flavour in order to get the most reliable ages and masses. This was attempted by obtaining the dust-reddening  $E(B - V)$  maps from Schlegel et al. (1998)<sup>8</sup>, using the Python script `dustmaps`<sup>9</sup> (Green 2018), and correcting the most reddened regions ( $E(B - V) > 0.1$ ), as done in Bonifacio et al. (2000). These were then converted into  $A_V$ , assuming  $R_V = 3.1$ , and then to  $A_J$ ,  $A_H$ ,  $A_{K_s}$ , and  $A_G$ , following the adopted PARSEC 3.5 extinction coefficients of Cardelli et al. (1989) and O’Donnell (1994), and the *Gaia* EDR3 passbands of Rielo et al. (2021), as summarised in Table 2. Finally, these extinctions were compared with the uncertainties of the absolute magnitudes in each respective band, as derived from Eq. (7).

To compile our final, adopted, catalogue (labelled without any underscore in Table A.1), we selected, for a given star, the projection flavour according to the following scheme:

- `speck` where  $A_{K_s} \leq \sigma_{M_{K_s}}$ , or  $r \leq 300$  pc and  $A_V \leq 3$  mag.
- `specjhk` where  $A_J \leq \sigma_{M_J}$  or  $r \leq 100$  pc.
- `specjhkg` where  $A_G \leq \sigma_{M_G}$  or  $r \leq 50$  pc.
- `spec` otherwise.

The resulting age and mass distributions of the compiled sample are shown in black in Fig. 7. The conditions regarding the distance and  $A_V$  are empirical, and take into account the fact that Schlegel’s values are the total extinctions along the line of sight, and that the Sun resides within a local bubble with very little extinction (Fitzgerald 1968; Lallement et al. 2014). The extinction criterion is an educated guess resulting from the analysis of Sect. 2.4 using reddened projections of synthetic data. Figure 8 shows the number of stars in bins of Galactic ( $\ell, b$ ) where each projection flavour is adopted. The `spec` flavour is, as expected, selected only for stars within the Galactic plane, and the `speck` flavour is the one that contains the most stars. Finally, the `specjhkg` flavour contains the smallest number of stars; however, they are spread all over ( $\ell, b$ ).

Figure 9 shows Kiel diagrams colour-coded by either metallicity, age, or initial mass, with the input  $T_{\text{eff}}$  and  $\log g$  (top row) and the output values (bottom row). These plots show that the parameters we recover in different regions of the diagram are compatible with what is expected: low-mass stars are mainly cool dwarfs, and old stars are at the redder part of the RGB. Similarly, the turn-off region contains significantly younger stars.

To conclude, we note that in the published catalogue (see Table A.1) the parameters resulting from this compilation are labelled without underscores. However, the results from each separate flavour are also published, with the appropriate and explicit label name. These can be particularly useful for the users who wish to adopt their own criteria to combine the different projections or who desire to adopt only one projection type for further probabilistic inferences. In the latter case, we recommend using the `speck`, `specjhk`, or `specjhkg` projections either by

limiting the study in a given volume (e.g. within the suggested cut-off distances,  $r$ , given at the beginning of this subsection) or if the aim is for a big volume, by deliberately adopting the `speck` projection (making sure to avoid regions at small  $|b|$ ) since it also provides reliable results in regions of low extinction (albeit with larger error bars).

## 2.7. Validation of the ages and masses

To validate our ages and masses we compare our results with the APOKASC-2 asteroseismic values (Pinsonneault et al. 2018), which cover a wide metallicity range ( $-2.5 \leq [\text{M}/\text{H}] \leq 0.5$  dex) but only giants ( $\log g < 3.3$ ), and the values from Casagrande et al. (2011), which deal mostly with main-sequence stars. We also compare the mean ages we derive for open clusters with those of Cantat-Gaudin et al. (2020), and perform a similar exercise for globular clusters based on the selection of Gaia Collaboration (2018c). Finally, we compare the values we obtain with those of the FLAME pipeline for the entire sample. In the subsections that follow, we always remove the stars that have a renormalised unit weight error (RUWE) greater than 1.4 as they could potentially be non-single sources (see Lindegren 2018), as well as the stars with GSP-Spec `KMgiant Par_flag` > 0.

### 2.7.1. Comparison with APOKASC-2 and Casagrande et al. (2011) ages and masses

We required the 12 first GSP-Spec parameter quality flags to be smaller than or equal to one (i.e. very good-quality sample with the small atmospheric parameter uncertainties) and selected stars with relative output age uncertainties smaller than 50 per cent. The mean offset and standard deviations between the GSP-Spec atmospheric parameters and the literature values are respectively for  $T_{\text{eff}}$ ,  $\log g$ , and  $[\text{M}/\text{H}]$ :  $-20 \pm 100$  K,  $0.01 \pm 0.21$  dex,  $-0.11 \pm 0.09$  dex for the APOKASC-2 sample, and  $-74 \pm 132$  K,  $-0.06 \pm 0.17$  dex,  $-0.17 \pm 0.13$  dex for the Casagrande et al. (2011) sample.

The blue lines in Fig. 10 show the running median in bins of reference catalogue values (i.e. APOKASC-2 or Casagrande et al. 2011) for the compiled sample defined in Sect. 2.6.2. For comparison purposes, running medians obtained when considering the FLAME-Spec and FLAME-Phot datasets are also shown in red and orange<sup>10</sup>.

We manage to reproduce adequately the literature ages, with mean offsets and standard deviations between the literature and the derived values of  $(-0.77 \pm 3.4)$  Gyr for APOKASC-2 and  $(-2.4 \pm 2.6)$  Gyr for Casagrande et al. (2011). These values drop to  $(0.2 \pm 2.3)$  Gyr and  $(-1.5 \pm 2.3)$  Gyr when we impose differences between the GSP-Spec atmospheric parameters and the literature values smaller than 150 K, 0.15 dex, and 0.1 dex for  $T_{\text{eff}}$ ,  $\log g$ , and  $[\text{M}/\text{H}]$ , respectively.

We find that the ages for the giants tend to be slightly overestimated until  $\tau \sim 11$  Gyr, above which value the median trend shows an underestimation of the ages. The first reason for this is that ages for old giants are inherently difficult to determine accurately because the isochrones are close to each other. Furthermore, since we do not have isochrones older than 13.7 Gyr, our code tends to sample the ages asymmetrically, leading to a larger selection of young isochrones compared to old ones.

<sup>8</sup> This choice is motivated by the fact that other dust maps, e.g. Green et al. (2019), either do not cover the entire sky or do not probe the entire *Gaia*-RVS volume.

<sup>9</sup> <https://dustmaps.readthedocs.io/en/latest/>

<sup>10</sup> For the FLAME-Spec and FLAME-Phot sample, we also impose metallicities to be greater than  $-0.5$  dex, as suggested by Fouesneau et al. (2023).

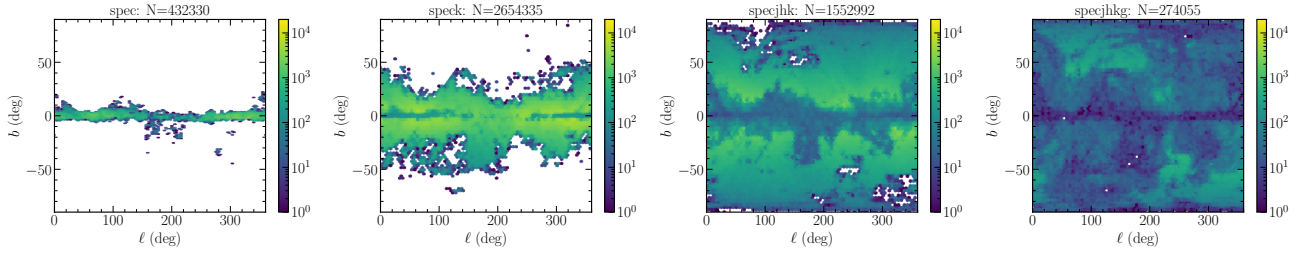


**Fig. 8.** Spatial distribution, in galactic sky-coordinates ( $l$ ,  $b$ ), of the number of stars for which we adopt each projection flavour. The total of selected stars and the considered projection are indicated at the top of each plot. Only targets with GSP-Spec KMgiantPar\_flag= 0 are considered here.

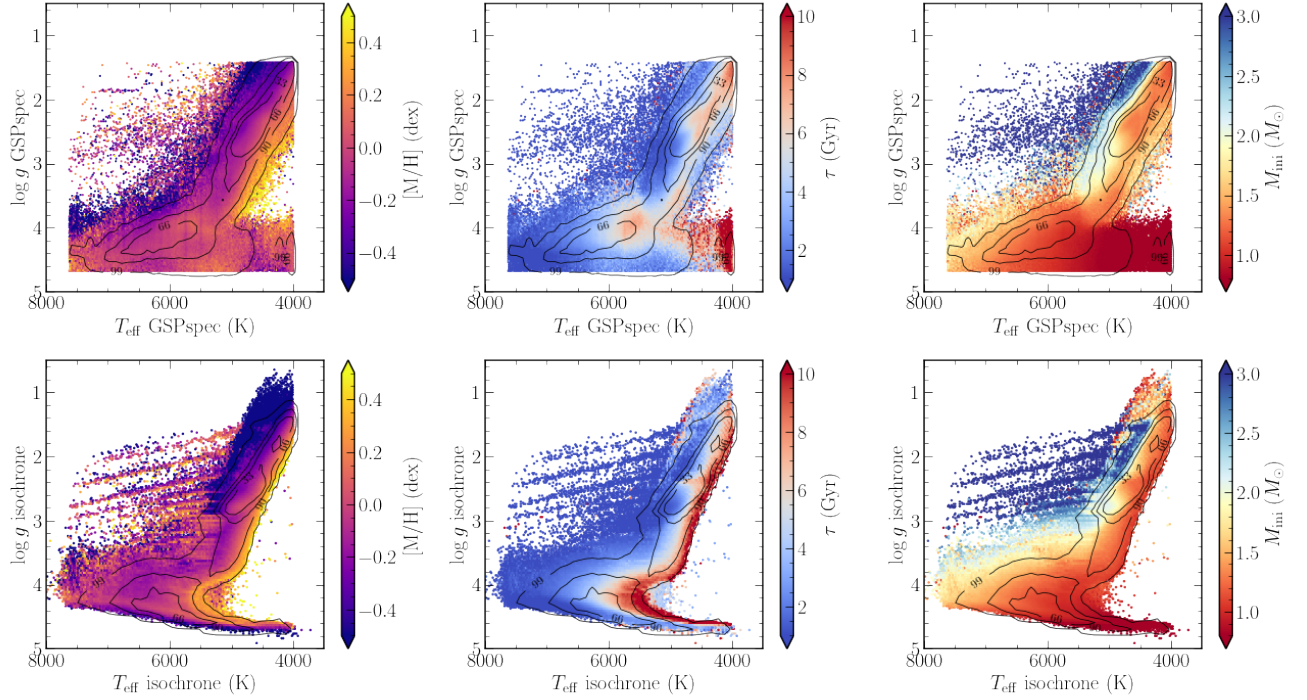


**Fig. 9.**  $T_{\text{eff}}$ - $\log g$  diagrams adopting GSP-Spec parameters (*top*) and isochrone-projected parameters (*bottom*). The colour-coding represents GSP-Spec calibrated metallicity, age (in Gyr), and initial stellar mass (in  $M_{\odot}$ ). Only targets with the first 12 quality GSP-Spec flags  $\leq 1$  and KMgiantPar\_flag=0 are considered here.

Additionally, we note that we have a relatively large disagreement on the ages of the youngest stars of Casagrande et al. (2011). Whereas it is not clear what the origin of this large disparity is, we see that we also find a similar trend with FLAME-Spec and FLAME-Phot parameters, the latter being based on completely different input parameters.

For the masses, we find a very good agreement, both for APOKASC-2 and Casagrande et al. (2011), with a slight overestimation of the masses for subsolar mass giants, and a slight underestimation for stars with masses greater than  $\sim 1.5 M_{\odot}$ . The mean offsets and standard deviations between the literature and the derived values are of  $(0.00 \pm 0.3) M_{\odot}$  for APOKASC-2 and  $(0.1 \pm 0.1) M_{\odot}$  for Casagrande et al. (2011). These values become  $(-0.1 \pm 0.2) M_{\odot}$  and  $(0.09 \pm 0.08) M_{\odot}$  when we impose differences between the GSP-Spec atmospheric parameters and the literature values lower than 150 K, 0.15 dex, and 0.1 dex for  $T_{\text{eff}}$ ,  $\log g$ , and  $[M/H]$ , respectively.

### 2.7.2. Open cluster ages

We selected from the sample of Cantat-Gaudin et al. (2020) the stars that have a published probability higher than 95 per cent

of being part of a considered open cluster. We furthermore filtered out the stars that have GSP-Spec flags greater than 1 and output relative age uncertainties greater than 50 per cent. From the resulting sample we computed the mean ages and dispersion per cluster and compared these numbers to the values published by Cantat-Gaudin et al. (2020). The results are shown in Fig. 11. They suggest that we perform very well for the young targets, with a small overestimation of the ages by 0.6 Gyr and an inner cluster age dispersion of the order of  $\sim 1$  Gyr for most of the objects that contain at least some turn-off or subgiant stars.

Amongst the few clusters for which the disagreement with the literature values is greater than 50 per cent (dashed lines in Fig. 11), we can identify two different cases. On the one hand, we have the clusters that contain mostly main-sequence stars, known to poorly constrain the age (see the case of Melotte25 in Fig. C.1). On the other hand, we have the objects for which we suspect that the input parameters could be slightly biased, since our proposed solution fits better the observed parameters than the isochrone with the literature age. These biases can either be due to a metallicity calibration that is different to that for field stars (see Fig. 13 of Recio-Blanco et al. 2023) or due to large uncertainties on the distance modulus. The open

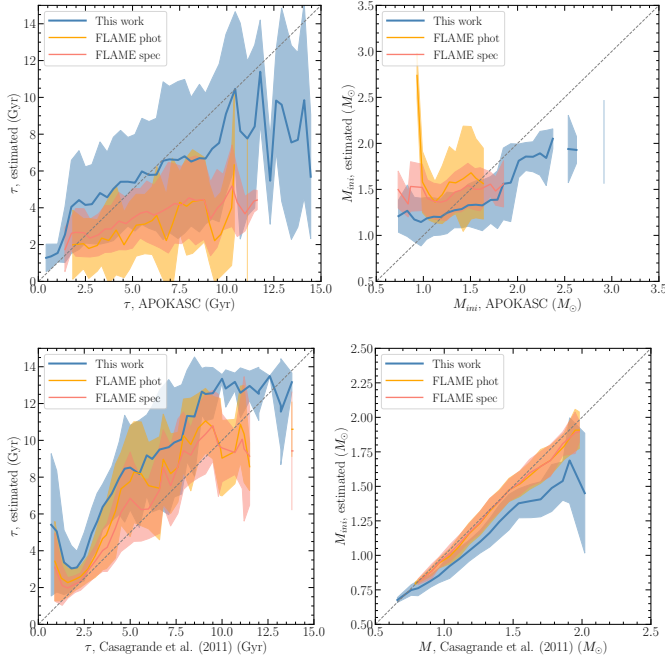


**Fig. 10.** Comparison of the derived ages (*left*) and masses (*right*) with the APOKASC-2 (*top*) and Casagrande et al. (2011), (*bottom*) catalogues. Plots show running medians in bins of reference (catalogue) values. In blue are shown the values derived with the compiled catalogue of Sect. 2.6.2. In red and orange are shown the results of the FLAME-Spec and FLAME-Phot modules, respectively. Shaded areas represent  $\pm 1\sigma$  around the running medians. Only the targets that have GSP-Spec flags equal to zero and relative age uncertainties (on each module separately) smaller than 50 per cent are selected. Additional cuts, imposing  $[M/H] > -0.5$  dex, are applied for the FLAME results.

cluster NGC2112 likely falls into this category, with a discrepancy with the literature estimations of  $\sim 5$  Gyr (Carraro et al. 2002; Kharchenko et al. 2013; Cantat-Gaudin et al. 2020).

### 2.7.3. Globular cluster ages

We investigated the performance of our code for old and metal-poor stars (i.e. stars belonging to globular clusters). This regime is known to be difficult to obtain ages for field stars as the isochrones, especially for giants, are very close to one another. We selected the globular cluster targets compiled in Gaia Collaboration (2018c) and cross-matched them with our sample, requiring GSP-Spec quality flags on the atmospheric parameters to be less than or equal to 1. Furthermore, the median S/N of the selected spectra being low, of the order of 30, we required that the differences between the input and output  $T_{\text{eff}}$ ,  $\log g$ , and  $[M/H]$  to be less than 200 K, 0.3, and 0.1 dex in order to ensure that we have measurements close to the isochrones. For the six globular clusters that contained at least three stars fulfilling the conditions above, we computed the mean age, with the expectation of finding them older than 10 Gyr (e.g. Vandenberg et al. 2013).

Despite the adopted age-prior for the metal-poor stars, we find ages ranging between 3.5 Gyr and 9.3 Gyr, consistent with the results given in Sect. 2.7.1 for APOKASC-2, which suggests that old targets tend to have underestimated ages. A closer investigation of the Kiel and  $T_{\text{eff}}-M_{K_s}$  diagrams (see Fig. C.2) highlights the difficulty of determining these ages properly due to the proximity of the various isochrones. In addition to this chal-

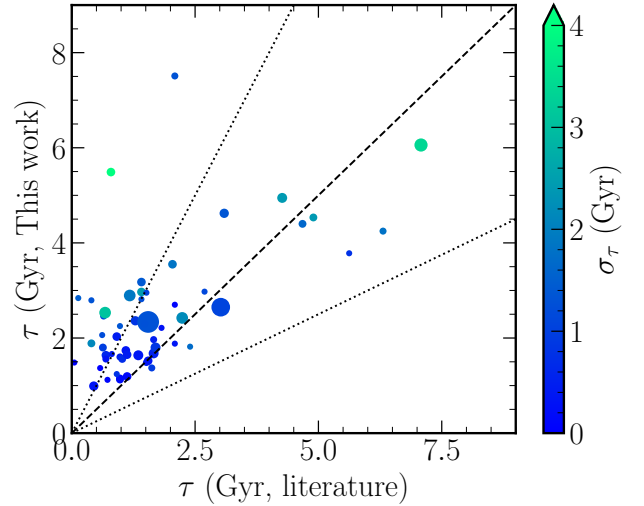


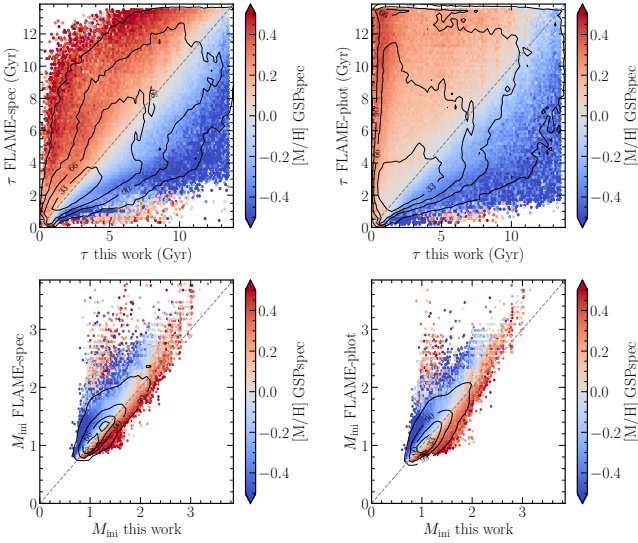
**Fig. 11.** Comparison of median open cluster ages with those of Cantat-Gaudin et al. (2020). The colour-coding corresponds to the age dispersion obtained within the cluster, and the size of the points is proportional to the number of cluster members that made our selection. A minimum of three stars per cluster is imposed. The dashed diagonal line represents the 1:1 relation, whereas the dotted lines show deviations from identity of  $\pm 50$  per cent.

lenge, we find that the mean metallicity of the stars within each cluster tend to differ by  $\sim +0.15$  dex compared to, for example, the values reported by Vandenberg et al. (2013). This metallicity difference, also noted in Gaia Collaboration (2023a), but without suggesting a specific calibration for these objects, is also partially responsible for the age offsets we find compared to expectations.

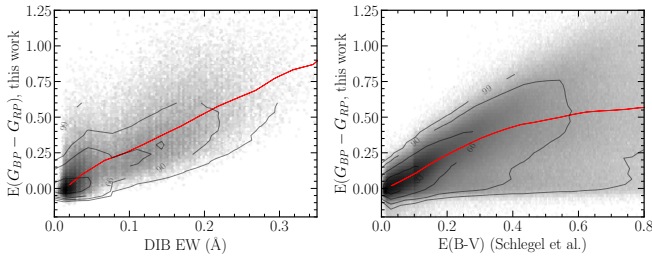
### 2.7.4. Comparison with FLAME ages and masses

Figure 12 compares our ages and masses with those derived from FLAME, obtained either with GSP-Phot input (i.e. FLAME-Phot) or with uncalibrated GSP-Spec (i.e. FLAME-Spec). We recall that our age and mass values, regardless of whether photometry is taken into account or not, are always estimated with the GSP-Spec  $T_{\text{eff}}$ , and the calibrated values of GSP-Spec for  $\log g$  and for  $[M/H]$ . To obtain this plot, only turn-off stars were selected (based on calibrated GSP-Spec parameters) since the FLAME results are less reliable for the giants (see Creevey et al. 2023; Fouesneau et al. 2023). We also imposed GSP-Spec parameter flags smaller than or equal to 1, and relative age uncertainties (based on the different age estimations) smaller than 50 per cent.

The agreement of FLAME with our age and mass values can be considered as adequate only for metallicities close to solar values. Figure 12 shows that as soon as  $[M/H]$  is different from zero, then the disagreement becomes non-negligible. For stars with  $[M/H] = \pm 0.15$  dex, we find mean age offsets of  $0.09 \pm 1.29$  Gyr and  $-0.01 \pm 1.40$  Gyr compared to FLAME-Spec and FLAME-Phot, respectively. These values increase to  $1.68 \pm 1.60$  Gyr and  $1.63 \pm 1.76$  Gyr when considering stars with  $[M/H] < -0.15$  dex and  $2.96 \pm 1.82$  Gyr and  $2.96 \pm 1.89$  Gyr for stars with  $[M/H] < -0.5$  dex. We therefore constrain to an even narrower metallicity range the statement found in Fouesneau et al. (2023) that suggests treating with caution the FLAME ages for stars with  $[M/H] \leq -0.5$  dex, and suggest keeping only the stars with  $[M/H] \pm 0.15$  dex around solar values.



**Fig. 12.** Comparison of the ages (top) and the masses (bottom) between the estimations obtained in this work and with those of FLAME-Spec (left) and FLAME-Phot (right). Only GSP-Spec turn-off stars with the first 13 GSP-Spec flags equal to zero are selected here, with age uncertainties (both in our code and the FLAME modules) smaller than 50 per cent. Contour lines contain 33, 66, 90, and 99 per cent of the distribution. The colour-coding is the GSP-Spec calibrated  $[M/H]$ .



**Fig. 13.** Comparison of  $E(G_{BP} - G_{RP})$  derived in this work, with the equivalent widths of diffuse interstellar bands at 862 nm derived from the same GSP-Spec spectra (left) and the Schlegel et al. (1998)  $E(B-V)$  with the Bonifacio et al. (2000) correction (right). For both plots, the grey colour-scale is the logarithm of the number of stars in one bin, and the red lines represent the running median. Overall, the correlations in both cases are very good.

### 2.8. Calculation of the reddening and the extinction

To derive the extinctions it is first necessary to compute the reddening  $E(G_{BP} - G_{RP})$ , obtained by measuring the difference between the projected and the observed colours ( $G_{BP} - G_{RP}$ ). Extinction,  $A_G$ , is then computed using

$$A_G = c_\theta \cdot E(G_{BP} - G_{RP}), \quad (9)$$

where  $c_\theta$  is a constant that depends on the stellar type<sup>11</sup> (Creevey et al. 2023; Foesneau et al. 2022).

The left plot of Fig. 13 compares the reddening  $E(G_{BP} - G_{RP})$  derived in our work, with the equivalent widths of the diffuse interstellar band at  $\sim 862$  nm, as derived in Gaia Collaboration (2023b). The right plot is a comparison with the Schlegel et al. (1998)  $E(B-V)$  reddening (corrected as described in Sect. 2.6.2 towards the regions with the largest extinction).

<sup>11</sup> For extinction converters as a function of the passband and the stellar atmospheric parameters see <https://www.cosmos.esa.int/web/gaia/dr3-astrophysical-parameter-inference>

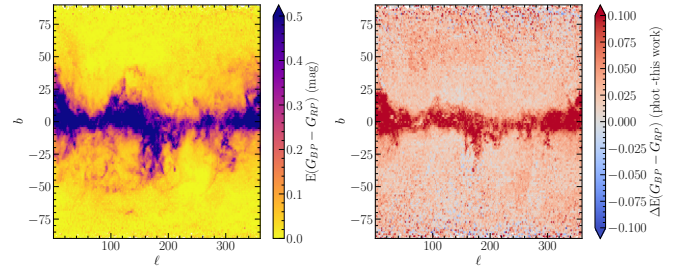


**Fig. 14.** Galactic  $(\ell, b)$  maps of the  $E(G_{BP} - G_{RP})$  distribution (left) and the residuals between the  $E(G_{BP} - G_{RP})$  estimation from GSP-Phot and our values (right).

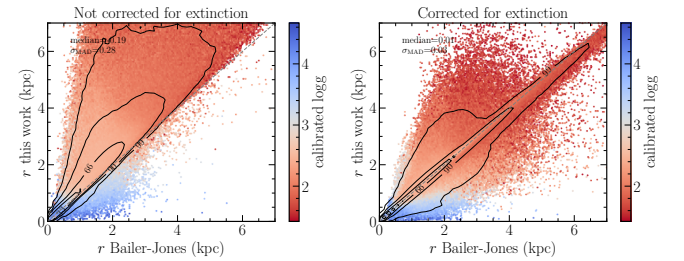


**Fig. 15.** Comparison of the line-of-sight distances derived from the projected  $M_G$  and extinction, with the geometric values from Bailer-Jones et al. (2021). No cuts in the uncertainties on the Bailer-Jones et al. (2021) distances or in our line-of-sight distances are made.

Overall, a good correlation is found with the two dust proxies, confirming our estimations of reddening. We note, however, that some of our targets have  $E(G_{BP} - G_{RP})$  values lower than zero. We decided not to artificially put them equal to zero, but note that the associated uncertainties of these stars should be considered.

The left plot of Fig. 14 shows the reddening map derived for the sample. The right plot of the same figure shows the residuals between the GSP-Phot  $E(G_{BP} - G_{RP})$  values and ours. The median difference above and below Galactic latitudes of  $|b| = 20^\circ$  is 0.019 mag and 0.052 mag, respectively. The agreement is rather good, acknowledging that GSP-Phot does not use the same input data or parameters as we do, and that it is precisely towards highly reddened regions that degeneracies between  $E(BP - RP)$  and  $T_{\text{eff}}$  make the GSP-Phot parametrisation challenging.

### 2.9. Absolute magnitudes and line-of-sight distances

Finally, to validate more thoroughly the projected absolute magnitudes, we compare the geometric line-of-sight distances,  $r$ , of Bailer-Jones et al. (2021) with those derived via the distance modulus (correcting for the projected extinctions, assuming  $c_\theta = 1.83037$ , valid for solar-type stars  $\pm 1500$  K). The results are shown in Fig. 15 (left, before correcting for the extinction, and right, after applying the correction). They suggest that we find a very good agreement between the two distance estimations, with a null median residual and a dispersion of 20 pc. We find that the one per cent of stars that have the largest disagreement with the Bailer-Jones et al. (2021) distances also have either large differences between the input  $\log g$  and the projected one ( $>0.3$ ) if these stars are dwarfs or large age uncertainties (larger than 50 per cent) if these stars are giants.

Finally, we note that the very good agreement that is found is not necessarily a direct consequence of the use of  $r$  when projecting the absolute magnitudes. We recall that when we project the absolute magnitudes, extinction is ignored. As can be seen in the left plot of this figure (which does not correct for the derived interstellar reddening), when the estimated  $A_G$  is neglected when computing the distance, the agreement between the two distance estimates is rather poor and biased.

### 3. Age and mass correlations with the orbital parameters and the positions in the Galaxy

In this section we illustrate the quality and the limitations of our projected parameters. To do so, we first compute the orbital parameters for all of the stars with measured radial velocities from the RVS and available astrometry. Then we correlate them with the stellar ages and masses for a high-quality GSP-Spec sample, requiring the first 12 quality flags of GSP-Spec to be smaller than or equal to one (except `fluxNoise_flag`, which we require to be smaller than or equal to 2); the `KMgiantPar_flag`, which we require equal to zero; and the relative age uncertainty, which we require to be smaller than 50 per cent.

#### 3.1. Determination of galactocentric positions, velocities, and orbital parameters

The galactocentric positions  $X, Y, Z$  (in Cartesian coordinates),  $R$  (galactocentric cylindrical radius), and cylindrical velocities (radial  $V_R$ , azimuthal  $V_\phi$ , vertical  $V_Z$ ) in a right-handed frame were computed for all of the stars that have a *Gaia* radial velocity measured ( $\sim 33$  million targets). In order to do so, we used the star's right ascension, declination, line-of-sight velocity, proper motions, and [Bailer-Jones et al. \(2021\)](#) EGDR3 geometric and photogeometric Bayesian line-of-sight distances (therefore leading to two sets of positions, velocities, and orbits). The assumed solar position is  $(R, Z)_\odot = (8.249, 0.0208)$  kpc ([GRAVITY Collaboration 2020](#); [Bennett & Bovy 2019](#)), and the velocities are  $(V_R, V_\phi, V_Z)_\odot = (-9.5, 250.7, 8.56)$  km s $^{-1}$  ([Reid & Brunthaler 2020](#); [GRAVITY Collaboration 2020](#)).

To compute the orbital parameters (actions, eccentricities, apocentre, pericentre, maximum distance from the Galactic plane), we used the *Stäckel fudge* method ([Binney 2012](#); [Sanders & Binney 2016](#); [Mackereth & Bovy 2018](#)) with the *Galpy* code ([Bovy 2015](#)), in combination with the axisymmetric potential of [McMillan \(2017\)](#) (adjusted to our adopted solar position and the local standard of rest velocity). The lower and upper confidence limits (corresponding to the 16th and 84th percentiles) were obtained by propagating the uncertainties of the line-of-sight distance, line-of-sight velocity, and proper motions using 20 Monte-Carlo realisations. No correlation between proper motions and distance uncertainties were taken into account, and we assumed a non-Gaussian distribution for  $r$ , constructed as two half-Gaussians defined by the upper and lower confidence limits of  $r$ .

#### 3.2. Galactic maps of ages and masses and identification of the spiral arms

Maps of the stellar ages and masses in Galactic Aitoff projection ( $\ell, b$ ) are shown in Fig. 16. Young and massive stars are predominantly found in (or close to) the Galactic plane, within the regions of high reddening (see Fig. 14), as expected from the

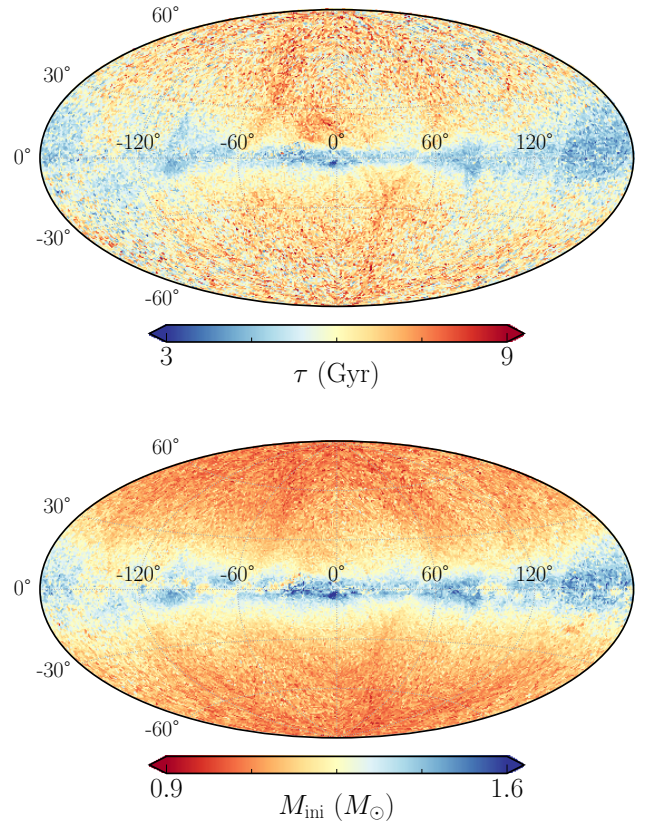


**Fig. 16.** Healpix projections (NSIDE=64) of the mean ages (top) and masses (bottom) for the compiled sample.

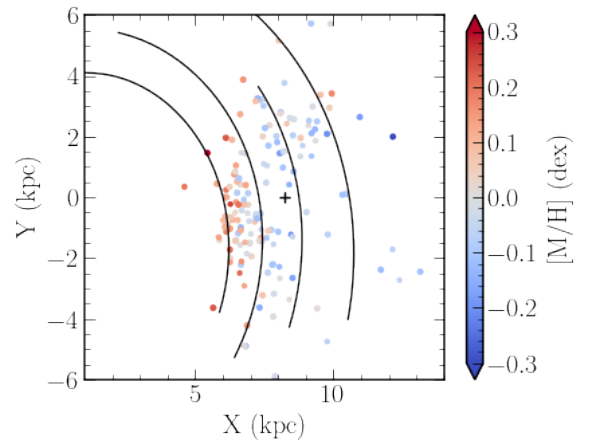


**Fig. 17.** Galactocentric Cartesian XY projection of the position of the stars having  $M_{\text{ini}} \geq 4 M_\odot$ ,  $\log g < 2$ , and  $Z_{\text{max}} < 0.5$  kpc. The Galactic centre is located at  $(X, Y) = 0$  (on the left) and Galactic rotation is going clockwise. The colour-coding represents the metallicity of the stars, whereas the plus sign is located at the Sun's position. The position of the Perseus, Local, Sagittarius, and Scutum spiral arms, based on the [Castro-Ginard et al. \(2021\)](#) results, are also plotted as black continuous lines.

interstellar medium distribution in the Milky Way (e.g. [Kalberla & Kerp 2009](#), and references therein).

In Fig. 17 we plot the galactocentric Cartesian X-Y positions of stars that have an estimated initial mass greater than 4 solar masses,  $\log g < 2$  (to avoid massive main-sequence stars at the solar vicinity) and a maximum distance from the galactic plane during their orbit (i.e.  $Z_{\text{max}}$ ) less than 0.5 kpc. Superimposed,

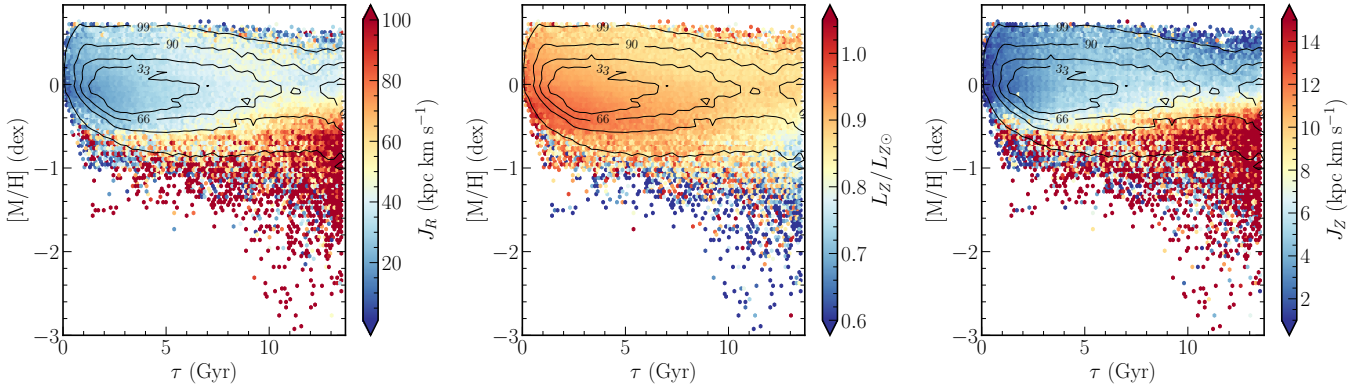


**Fig. 18.** Age-metallicity relations as a function of the radial and vertical actions ( $J_R$ ,  $J_Z$ , first and third panel, respectively) and normalised angular momentum ( $L_Z$  normalised by the Sun's value, middle panel) for stars closer than 1 kpc from the Sun.

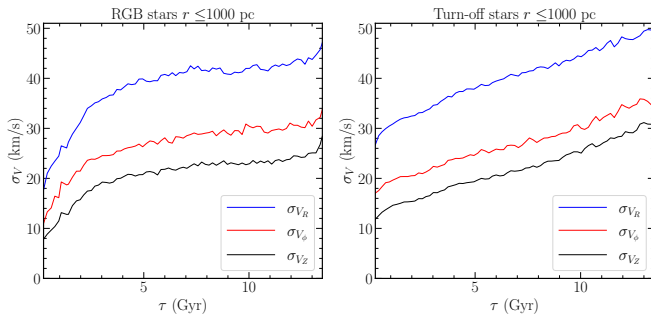


**Fig. 19.** Age-velocity dispersion for the RGB stars (*left*) and for the turn-off stars (*right*) closer than 1 kpc from the Sun. A clear trend is found in both samples, for each velocity component. However, the fact that these trends do not exhibit the same shape, highlights the different precisions achieved for each stellar type: RGB stars tend to have underestimated ages for old stars, whereas the younger turn-off stars tend to have overestimated ages.

we also plot the position of the Perseus, Local, Sagittarius, and Scutum spiral arms, based on the [Castro-Ginard et al. \(2021\)](#) analysis of open clusters with *Gaia* EDR3 data (adapted to match our assumed solar position). The positions of the massive stars follow very closely the positions of the modelled spiral arms, consistent with the fact that the latter are regions where star formation takes place. Furthermore, one can also see the clear metallicity gradient within those stars, reflecting the metallicity of the interstellar medium at these locations (as these stars are found to be younger than 300 Myr).

### 3.3. Age-metallicity relation as a function of orbital actions

Figure 18 shows the age metallicity-relation we derive for the stars within 1 kpc from the Sun, colour-coded by the three different computed actions. Overall, we find a flat trend over the entire age-range, in agreement with previous studies (e.g. [Edvardsson et al. 1993](#); [Casagrande et al. 2011](#); [Bergemann et al. 2014](#); [Feillet et al. 2019](#)). Young stars ( $\tau \lesssim 2$  Gyr) of subsolar metallicity tend to have low  $J_R$  and  $L_Z/L_{Z\odot}$  above one, compatible with stars visiting the solar neighbourhood on slightly eccentric orbits from the outer disc (we find that these stars have  $e < 0.1$ ).

Super-solar metallicity stars are found at all ages, with perhaps a slight decrease in their number for ages above 10 Gyr that may be due to our age prior. However, it is worth noting that

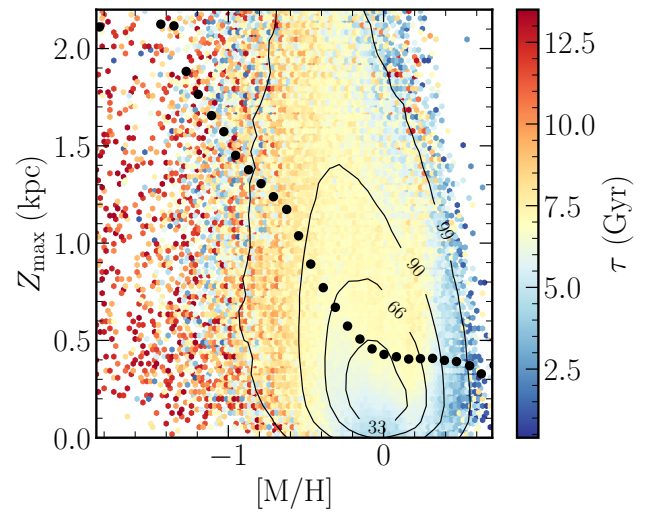


**Fig. 20.** Maximum distance from the Galactic plane reached during a star's orbit ( $Z_{\max}$ , in kpc) vs. metallicity, colour-coded by age (in Gyr). A clear increase in  $Z_{\max}$  as a function of metallicity and age can be seen from the black dots on the figure that represent the running mean. This trend is compatible with what is expected for a transition between thin and thick discs and between thick disc and halo.

whereas the youngest super-solar metallicity stars have low  $J_R$  and  $L_Z/L_{Z\odot}$  close to 0.9, the older stars have on average a larger radial action and more eccentric orbits ( $e > 0.3$ ), suggesting that they just visit the solar neighbourhood, while being close to their apocentre. Interestingly, we also find old ( $\tau > 8$  Gyr) metal-rich stars with normalised angular momentum around one and low values of radial and vertical actions. These stars are obvious candidates of objects having experienced churning processes, i.e. stars that moved far from their birthplace without changing their eccentricity via corotation resonances with the spiral arms or the Galactic bar ([Schönrich & Binney 2009](#); [Minchev et al. 2013](#); [Kordopatis et al. 2015a](#)).

Finally, we find that metal-poor stars ( $[M/H] < -1$  dex) within 1 kpc from the Sun are predominantly old, with large radial and vertical actions and low angular momenta, as is expected for typical halo stars.

### 3.4. Age-velocity dispersion and $Z_{\max}$ -metallicity relations

Figure 19 shows the age-velocity dispersion relation of our RGB sample (left) and our turn-off sample (right), for stars closer

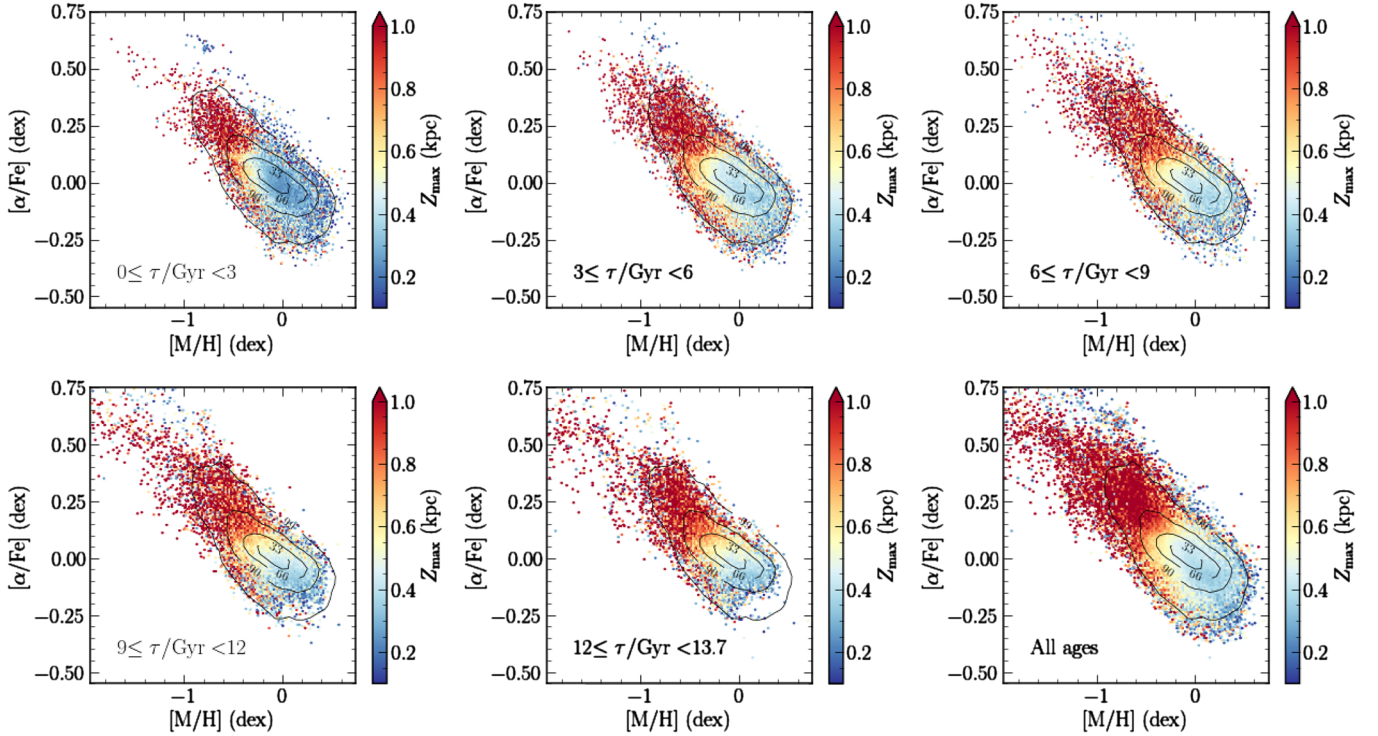


**Fig. 21.** Calibrated  $[\alpha/\text{Fe}]$  vs.  $[\text{M}/\text{H}]$ , in 3 Gyr age bins for giant stars ( $\log g < 3.5$ ) closer than 1.5 kpc from the Sun. The contour lines inside each panel were evaluated for the sample considering all the age ranges, represented in the bottom right panel. The colour-coding corresponds to the maximum distance above the Galactic plane that a star can reach during its orbit.

than 1 kpc from the Sun. In agreement with previous results (e.g. [Aumer & Binney 2009](#)), we find a clear increase in the velocity dispersions with age, which is even more pronounced when selecting only the turn-off stars. The trend for old stars is starker for the turn-off sample, whereas the giants seem to have a stronger trend at the young side. These different behaviours are in agreement with those described in Sect. 2.7 using the APOKASC-2 and [Casagrande et al. \(2011\)](#) datasets, which suggests that old giants tend to have underestimated ages, whereas very young turn-off stars tend to have overestimated ages.

Similarly, Fig. 20 shows the maximum distance from the Galactic plane reached during a star's orbit as a function of metallicity, colour-coded by age. The black circles represent the running mean in bins of  $[\text{M}/\text{H}]$ . It can be seen that stars with metallicities greater than  $-0.2$  dex tend to be young ( $\tau < 5$  Gyr) and confined in a thin-disc configuration ( $Z_{\text{max}} < 0.3$  kpc), whereas stars with  $-0.2 < [\text{M}/\text{H}] < -1$  dex have  $Z_{\text{max}} < 1.1$  kpc and are globally younger than 10 Gyr, in agreement with the thick-disc properties in the solar neighbourhood (e.g. [Bensby et al. 2014](#); [Haywood et al. 2018](#)).

### 3.5. Chemical enrichment of the Galactic disc

A different way to show the wealth of information in our sample can be seen in Fig. 21, where we plot the  $[\alpha/\text{Fe}] - [\text{M}/\text{H}]$  space, in various age-bins, as a function of the orbital parameters (in this case,  $Z_{\text{max}}$ ). The  $[\alpha/\text{Fe}]$  of GSP-Spec, being mostly based on calcium abundance, does not allow us to separate the well-known thin- and thick-disc chemical sequences (see e.g. [Kordopatis et al. 2015b](#); [Hayden et al. 2015](#), obtained with high-resolution *Gaia*-ESO or APOGEE spectra); nevertheless, one can see that young stars mostly have low  $[\alpha/\text{Fe}]$  ratios ( $< 0.2$ ), high metallicity ( $> -0.5$ ), and low  $Z_{\text{max}}$ . As look-back time (i.e. age) increases, lower metallicity and higher  $[\alpha/\text{Fe}]$  regions

become populated, with the low-metallicity tail exhibiting the highest  $Z_{\text{max}}$  values. Chemical evolution models can then be fitted to these trends in order to determine the star formation history of the Galaxy together with its gas infall history.

In addition to the inner evolution of the Milky Way, our dataset also allows us to probe accreted populations present in the surveyed volume. For example, low-metallicity and low- $[\alpha/\text{Fe}]$  stars with high  $Z_{\text{max}}$  associated with *Gaia*-Enceladus-Sausage ([Belokurov et al. 2018](#); [Helmi et al. 2018](#)) stars are detected starting from  $\tau > 3$  Gyr (with possible traces even below that age), which we believe are subgiants with underestimated ages. Interestingly, the plot also shows some low-metallicity ( $[\text{M}/\text{H}] < -0.6$  dex)  $\alpha$ -enhanced ( $[\alpha/\text{Fe}] > 0.55$  dex) and low- $Z_{\text{max}}$  ( $< 0.3$  kpc) stars present at all age bins. We find that these stars are mostly targets with  $T_{\text{eff}} > 6000$  K and similar  $\log g \sim 3.5$  (also seen in the top left plot of Fig. 9). The true existence of these targets will have to be investigated further.

## 4. Conclusions

Using the calibrated atmospheric parameters derived from *Gaia* spectra and the GSP-Spec module, the photometry from 2MASS and *Gaia*-EDR3, and Bayesian line-of-sight distances estimated using *Gaia*-EDR3 parallaxes, we derived the ages, initial masses, and absolute magnitudes for  $\sim 5$  million targets in four different ways, depending on different combinations of parameters to project on isochrones, and based on PARSEC isochrones. We propose a way to combine these different estimations based on the extinction along the line of sight (see Sect. 2.6.2), and publish a compiled catalogue of best projected parameters and their uncertainties.

We note that the reliability of the projected parameters is closely related to that of the input data and their associated

uncertainties. Biases in  $T_{\text{eff}}$ ,  $\log g$ ,  $[M/H]$ , or distance modulus, and/or underestimated errors on them, may lead (depending on the stellar evolutionary phase) to biases on the output ages and masses. For this reason, a careful consideration of GSP-Spec's flags on the atmospheric parameters is necessary, according to the user's objectives, in order to choose the parameters with the desired reliability (see Table 2 in Recio-Blanco et al. 2023). Furthermore, close binaries and multiple stellar systems of moderate mass ratios, not caught by the RUWE parameter, may hamper our results despite the good GSP-Spec flags. These systems, the number of which is found to be anti-correlated with metallicity (e.g. Moe et al. 2019; El-Badry & Rix 2019; Price-Whelan et al. 2020), have brighter magnitudes (up to  $\sim -0.75$  mag, in the case of an unresolved binary system of two identical stars; see Gaia Collaboration 2018b), which usually results, for a target located before the turn-off, in an overestimation of its age (and vice versa if the star is located after the turn-off; see the behaviour of the isochrones in the upper and lower panels 2 of Fig. 1).

Tests made comparing our ages and masses with reference catalogues of field stars, open clusters, and globular clusters suggest that our code performs well, provided a filtering on the estimated relative age uncertainty (we suggest  $<50$  per cent), except for the older giants, whose ages tend to be underestimated. Ages are found to be the most reliable for turn-off stars, even when the GSP-Spec parameters have large uncertainties, whereas age estimations for giants and main-sequence stars are also retrieved reliably (with uncertainties of the order of 2 Gyr) provided the extinction towards the star's line of sight is less than  $A_V \lesssim 2.5$  mag. Initial stellar masses are retrieved robustly for main-sequence and turn-off stars (dispersions compared to literature values are of the order of  $0.1 M_{\odot}$ ), whereas a filtering based on the age uncertainty of the giants is necessary to obtain reliable masses for the latter (dispersions compared to the literature values are of the order of  $0.3 M_{\odot}$ ).

We complete our catalogue with galactocentric positions and velocities as well as orbital parameters (actions, eccentricities, apocentres, pericentres, maximum distance from the Galactic plane) evaluated for the entire RVS sample, using an axisymmetric Galactic potential and commonly used orbital derivation methods and codes. The catalogue, which is publicly available<sup>12</sup>, is described in Table A.1.

*Acknowledgements.* We thank the referee for a constructive interaction and report. M. Fouesneau and V. Hill are warmly thanked for valuable comments, as well as CU8 and CU9 members that helped validating the stellar parameters used in this paper. This work has made use of data from the European Space Agency (ESA) mission *Gaia* (<https://www.cosmos.esa.int/gaia>), processed by the *Gaia* Data Processing and Analysis Consortium (DPAC, <https://www.cosmos.esa.int/web/gaia/dpac/consortium>). Funding for the DPAC has been provided by national institutions, in particular the institutions participating in the *Gaia* Multilateral Agreement. This research made use of Astropy, a community-developed core Python package for Astronomy (Astropy Collaboration 2013, 2018). The Centre National de la Recherche Scientifique (CNRS) and its SNO *Gaia* of the Institut des Sciences de l'Univers (INSU), its Programmes Nationaux: Cosmologie et Galaxies (PNCG) are thanked for their valuable financial support. ARB, GK and ES acknowledge funding from the European Union's Horizon 2020 research and innovation program under SPACE-H2020 grant agreement number 101004214 (EXPLORE project). PM acknowledges support from the Swedish National Space Agency (SNSA) under grant 20/136. GK gratefully acknowledges support from the french national research agency (ANR) funded project MWDisc (ANR-20-CE31-0004).

## References

- Anders, F., Khalatyan, A., Chiappini, C., et al. 2019, *A&A*, 628, A94  
 Andrae, R., Fouesneau, M., Creevey, O., et al. 2018, *A&A*, 616, A8  
 Andrae, R., Fouesneau, M., Sordo, R., et al. 2023, *A&A*, in press, <https://doi.org/10.1051/0004-6361/202243462>  
 Astropy Collaboration (Robitaille, T. P., et al.) 2013, *A&A*, 558, A33  
 Astropy Collaboration (Price-Whelan, A. M., et al.) 2018, *AJ*, 156, 123  
 Aumer, M., & Binney, J. J. 2009, *MNRAS*, 397, 1286  
 Bailer-Jones, C. A. L. 2015, *PASP*, 127, 994  
 Bailer-Jones, C. A. L., Andrae, R., Arcay, B., et al. 2013, *A&A*, 559, A74  
 Bailer-Jones, C. A. L., Rybizki, J., Fouesneau, M., Demleitner, M., & Andrae, R. 2021, *AJ*, 161, 147  
 Basu, S., & Antia, H. M. 1997, *MNRAS*, 287, 189  
 Belokurov, V., Erkal, D., Evans, N. W., Koposov, S. E., & Deason, A. J. 2018, *MNRAS*, 478, 611  
 Bennett, M., & Bovy, J. 2019, *MNRAS*, 482, 1417  
 Bensby, T., Feltzing, S., & Oey, M. S. 2014, *A&A*, 562, A71  
 Bergemann, M., Ruchti, G. R., Serenelli, A., et al. 2014, *A&A*, 565, A89  
 Binney, J. 2012, *MNRAS*, 426, 1324  
 Binney, J., Burnett, B., Kordopatis, G., et al. 2014, *MNRAS*, 437, 351  
 Bonifacio, P., Monai, S., & Beers, T. C. 2000, *AJ*, 120, 2065  
 Bovy, J. 2015, *ApJS*, 216, 29  
 Bovy, J., Leung, H. W., Hunt, J. A. S., et al. 2019, *MNRAS*, 490, 4740  
 Bressan, A., Marigo, P., Girardi, L., et al. 2012, *MNRAS*, 427, 127  
 Caffau, E., Ludwig, H. G., Steffen, M., Freytag, B., & Bonifacio, P. 2011, *Sol. Phys.*, 268, 255  
 Cantat-Gaudin, T., Anders, F., Castro-Ginard, A., et al. 2020, *A&A*, 640, A1  
 Cardelli, J. A., Clayton, G. C., & Mathis, J. S. 1989, *ApJ*, 345, 245  
 Carraro, G., Barbon, R., & Boschetti, C. S. 2002, *MNRAS*, 336, 259  
 Casagrande, L., Schönrich, R., Asplund, M., et al. 2011, *A&A*, 530, A138  
 Castro-Ginard, A., McMillan, P. J., Luri, X., et al. 2021, *A&A*, 652, A162  
 Chen, Y., Bressan, A., Girardi, L., et al. 2015, *MNRAS*, 452, 1068  
 Creevey, O. L., Sordo, R., Pailler, F., et al. 2023, *A&A*, in press, <https://doi.org/10.1051/0004-6361/202243688>  
 Delchambre, L., Bailer-Jones, C. A. L., Bellas-Velidis, I., et al. 2023, *A&A*, in press, <https://doi.org/10.1051/0004-6361/202243423>  
 Demarque, P., Woo, J.-H., Kim, Y.-C., & Yi, S. K. 2004, *ApJS*, 155, 667  
 Dotter, A. 2016, *ApJS*, 222, 8  
 Dotter, A., Chaboyer, B., Jevremović, D., et al. 2008, *ApJS*, 178, 89  
 Edvardsson, B., Andersen, J., Gustafsson, B., et al. 1993, *A&A*, 275, 101  
 El-Badry, K., & Rix, H.-W. 2019, *MNRAS*, 482, L139  
 Feuillet, D. K., Frankel, N., Lind, K., et al. 2019, *MNRAS*, 489, 1742  
 Feuillet, D. K., Feltzing, S., Sahlholdt, C. L., & Casagrande, L. 2020, *MNRAS*, 497, 109  
 Fitzgerald, M. P. 1968, *AJ*, 73, 983  
 Fouesneau, M., Andrae, R., Sordo, R., & Dharmawardena, T. 2022, *dustapprox* <https://github.com/mfouesneau/dustapprox>  
 Fouesneau, M., Frémat, Y., Andrae, R., et al. 2023, *A&A*, in press, <https://doi.org/10.1051/0004-6361/202243919>  
 Freeman, K., & Bland-Hawthorn, J. 2002, *ARA&A*, 40, 487  
 Gaia Collaboration (Prusti, T., et al.) 2016a, *A&A*, 595, A1  
 Gaia Collaboration (Brown, A., et al.) 2016b, *A&A*, 595, A2  
 Gaia Collaboration (Brown, A., et al.) 2018a, *A&A*, 616, A1  
 Gaia Collaboration (Babusiaux, C., et al.) 2018b, *A&A*, 616, A10  
 Gaia Collaboration (Helmi, A., et al.) 2018c, *A&A*, 616, A12  
 Gaia Collaboration (Brown, A., et al.) 2021a, *A&A*, 649, A1  
 Gaia Collaboration (Antoja, T., et al.) 2021a, *A&A*, 649, A8  
 Gaia Collaboration (Recio-Blanco, A., et al.) 2023a, *A&A*, in press, <https://doi.org/10.1051/0004-6361/202243511>  
 Gaia Collaboration (Schultheis, M., et al.) 2023b, *A&A*, in press, <https://doi.org/10.1051/0004-6361/202243283>  
 Gaia Collaboration (Vallenari, A., et al.) 2023c, *A&A*, in press, <https://doi.org/10.1051/0004-6361/202243940>  
 GRAVITY Collaboration (Abuter, R., et al.) 2020, *A&A*, 636, L5  
 Green, G. 2018, *J. Open Source Softw.*, 3, 695  
 Green, G. M., Schlafly, E., Zucker, C., Speagle, J. S., & Finkbeiner, D. 2019, *ApJ*, 887, 93  
 Hayden, M. R., Bovy, J., Holtzman, J. A., et al. 2015, *ApJ*, 808, 132  
 Hayden, M. R., Recio-Blanco, A., de Laverny, P., Mikolaitis, S., & Worley, C. C. 2017, *A&A*, 608, L1  
 Haywood, M., Di Matteo, P., Lehnert, M. D., et al. 2018, *ApJ*, 863, 113  
 Helmi, A., Babusiaux, C., Koppelman, H. H., et al. 2018, *Nature*, 563, 85  
 Hidalgo, S. L., Pietrinferni, A., Cassisi, S., et al. 2018, *ApJ*, 856, 125  
 Jørgensen, B. R., & Lindegren, L. 2005, *A&A*, 436, 127  
 Kalberla, P. M. W., & Kerp, J. 2009, *ARA&A*, 47, 27  
 Kharchenko, N. V., Piskunov, A. E., Schilbach, E., Röser, S., & Scholz, R. D. 2013, *A&A*, 558, A53

<sup>12</sup> <http://www.astropy.org>



- Kordopatis, G., Recio-Blanco, A., de Laverny, P., et al. 2011, *A&A*, **535**, A107
- Kordopatis, G., Hill, V., Irwin, M., et al. 2013, *A&A*, **555**, A12
- Kordopatis, G., Binney, J., Gilmore, G., et al. 2015a, *MNRAS*, **447**, 3526
- Kordopatis, G., Wyse, R. F. G., Gilmore, G., et al. 2015b, *A&A*, **582**, A122
- Kordopatis, G., Amorisco, N. C., Evans, N. W., Gilmore, G., & Koposov, S. E. 2016, *MNRAS*, **457**, 1299
- Kordopatis, G., Recio-Blanco, A., Schultheis, M., & Hill, V. 2020, *A&A*, **643**, A69
- Lallement, R., Vergely, J. L., Valette, B., et al. 2014, *A&A*, **561**, A91
- Laporte, C. F. P., Belokurov, V., Koposov, S. E., Smith, M. C., & Hill, V. 2020, *MNRAS*, **492**, L61
- Leung, H. W., & Bovy, J. 2019, *MNRAS*, **483**, 3255
- Lindgren, L. 2018, *Re-normalising the Astrometric chi-square in Gaia DR2*, *GAIA-C3-TN-LU-LL-124*
- Luri, X., Brown, A. G. A., Sarro, L. M., et al. 2018, *A&A*, **616**, A9
- Mackereth, J. T., & Bovy, J. 2018, *PASP*, **130**, 114501
- Magrini, L., Randich, S., Kordopatis, G., et al. 2017, *A&A*, **603**, A2
- Magrini, L., Spina, L., Randich, S., et al. 2018, *A&A*, **617**, A106
- Marigo, P., Bressan, A., Nanni, A., Girardi, L., & Pumo, M. L. 2013, *MNRAS*, **434**, 488
- McMillan, P. J. 2017, *MNRAS*, **465**, 76
- McMillan, P. J., Kordopatis, G., Kunder, A., et al. 2018, *MNRAS*, **477**, 5279
- Miglio, A., Chiappini, C., Morel, T., et al. 2013, *MNRAS*, **429**, 423
- Minchev, I., Chiappini, C., & Martig, M. 2013, *A&A*, **558**, A9
- Moe, M., Kratter, K. M., & Badenes, C. 2019, *ApJ*, **875**, 61
- Myeong, G. C., Vasiliev, E., Iorio, G., Evans, N. W., & Belokurov, V. 2019, *MNRAS*, **488**, 1235
- Naidu, R. P., Conroy, C., Bonaca, A., et al. 2020, *ApJ*, **901**, 48
- O'Donnell, J. E. 1994, *ApJ*, **422**, 158
- Pastorelli, G., Marigo, P., Girardi, L., et al. 2020, *MNRAS*, **498**, 3283
- Pinsonneault, M. H., Elsworth, Y. P., Tayar, J., et al. 2018, *ApJS*, **239**, 32
- Price-Whelan, A. M., Hogg, D. W., Rix, H.-W., et al. 2020, *ApJ*, **895**, 2
- Queiroz, A. B. A., Anders, F., Santiago, B. X., et al. 2018, *MNRAS*, **476**, 2556
- Recio-Blanco, A., de Laverny, P., Kordopatis, G., et al. 2014, *A&A*, **567**, A5
- Recio-Blanco, A., de Laverny, P., Palicio, P. A., et al. 2023, *A&A*, in press, <https://doi.org/10.1051/0004-6361/202243750>
- Reid, M. J., & Brunthaler, A. 2020, *ApJ*, **892**, 39
- Riello, M., de Angeli, F., Evans, D. W., et al. 2021, *VizieR Online Data Catalog: J/A+A/649/A3*
- Rosenfield, P., Marigo, P., Girardi, L., et al. 2016, *ApJ*, **822**, 73
- Salaris, M., Chieffi, A., & Straniero, O. 1993, *ApJ*, **414**, 580
- Sanders, J. L., & Binney, J. 2016, *MNRAS*, **457**, 2107
- Sanders, J. L., & Das, P. 2018, *MNRAS*, **481**, 4093
- Santos-Peral, P., Recio-Blanco, A., Kordopatis, G., Fernández-Alvar, E., & de Laverny, P. 2021, *A&A*, **653**, A85
- Schlegel, D. J., Finkbeiner, D. P., & Davis, M. 1998, *ApJ*, **500**, 525
- Schönrich, R., & Binney, J. 2009, *MNRAS*, **396**, 203
- Schönrich, R., McMillan, P., & Eyer, L. 2019, *MNRAS*, **487**, 3568
- Schultheis, M., Kordopatis, G., Recio-Blanco, A., et al. 2015, *A&A*, **577**, A77
- Schultheis, M., Rojas-Arriagada, A., García Pérez, A. E., et al. 2017, *A&A*, **600**, A14
- Skrutskie, M. F., Cutri, R. M., Stiening, R., et al. 2006, *AJ*, **131**, 1163
- Soderblom, D. R. 2010, *ARA&A*, **48**, 581
- Stello, D., Saunders, N., Grunblatt, S., et al. 2022, *MNRAS*, **512**, 1677
- Tang, J., Bressan, A., Rosenfield, P., et al. 2014, *MNRAS*, **445**, 4287
- Valentini, M., Chiappini, C., Bossini, D., et al. 2019, *A&A*, **627**, A173
- VandenBerg, D. A., Brogaard, K., Leaman, R., & Casagrande, L. 2013, *ApJ*, **775**, 134
- Zhao, H., Schultheis, M., Recio-Blanco, A., et al. 2021, *A&A*, **645**, A14
- Zwitter, T., Matijević, G., Breddels, M. A., et al. 2010, *A&A*, **522**, A54

## Appendix A: Output catalogue format

Table A.1. Description of the columns of the published catalogue

Name of column	Description	Units
source_id	Gaia DR3 source ID	–
age	Inferred age	Gyr
age_error	Uncertainty on the inferred age	Gyr
m_ini	Inferred initial stellar mass	$M_{\odot}$
m_ini_error	Inferred uncertainty on the initial stellar mass	$M_{\odot}$
teff	Adopted projected $T_{\text{eff}}$	K
logg	Adopted projected $\log g$	dex
meta	Adopted projected [M/H]	dex
p_flavour	Adopted projection flavour for inferred ages and masses	
G	Inferred absolute G magnitude	mag
G_BP	Inferred absolute $G_{BP}$ magnitude	mag
G_RP	Inferred absolute $G_{RP}$ magnitude	mag
ebprp	Inferred reddening using the projected $G_{BP}$ and $G_{RP}$	mag
ebprp_error	Uncertainty on the inferred reddening	mag
**_spec	Parameters adopting the calibrated GSP-Spec parameters only	
**_speck	Parameters adopting the calibrated GSP-Spec parameters and the $K_s$ absolute magnitude	
**_specjkhk	Parameters adopting the calibrated GSP-Spec parameters and the $J, H, K_s$ absolute magnitudes	
**_specjhkg	Parameters adopting the calibrated GSP-Spec parameters and the $J, H, K_s, G$ absolute magnitudes	
x_med_dgeo	Median galactocentric Cartesian X position	kpc
y_med_dgeo	Median galactocentric Cartesian Y position	kpc
z_med_dgeo	Median galactocentric Cartesian Z position	kpc
r_med_dgeo	Median heliocentric line-of-sight distance with geometric prior from <a href="#">Bailer-Jones et al. (2021)</a>	pc
vr_med_dgeo	Median galactocentric radial velocity obtained using r_med_dgeo	$\text{km s}^{-1}$
vphi_med_dgeo	Median galactocentric azimuthal velocity obtained using r_med_dgeo	$\text{km s}^{-1}$
vz_med_dgeo	Median galactocentric vertical velocity obtained using r_med_dgeo	$\text{km s}^{-1}$
jr_med_dgeo	Median radial action obtained using r_med_dgeo	$\text{kpc km s}^{-1}$
jphi_med_dgeo	Median angular momentum (i.e. azimuthal action) obtained using r_med_dgeo	$\text{kpc km s}^{-1}$
jz_med_dgeo	Median vertical action obtained using r_med_dgeo	$\text{kpc km s}^{-1}$
zmax_med_dgeo	Median maximum distance from the galactic plane obtained using r_med_dgeo	kpc
rapo_med_dgeo	Median apogalactic radius reached by the star, obtained using r_med_dgeo	kpc
rperi_med_dgeo	Median perigalactic radius reached by the star, obtained using r_med_dgeo	kpc
e_med_dgeo	Median eccentricity, obtained using r_med_dgeo	kpc
**_upper_dgeo	Upper confidence limit of the parameters	
**_lower_dgeo	Lower confidence limit of the parameters	
**_dphotogeo	Parameters obtained using the photogeometric distances from <a href="#">Bailer-Jones et al. (2021)</a>	

## Appendix B: Results of the isochrone projection with extinction

Figures B.1 to B.3 are similar to Fig. 3. They consider only the speck, specjnhk, and specjnhkg projections, with Q50 uncertainties in  $T_{\text{eff}}$ ,  $\log g$ , and  $[M/H]$ , and uncertainties in  $J$ ,  $H$ ,  $K_s$ , and  $G$ , as indicated in the top left corner of each plot. The input magnitudes are reddened according to the extinction  $A_V$  labelled within each plot.

Figures B.1 to B.3 are similar to Fig. 3. They consider only the speck, specjnhk, and specjnhkg projections, with Q50 uncertainties in  $T_{\text{eff}}$ ,  $\log g$ , and  $[M/H]$ , and uncertainties in  $J$ ,  $H$ ,  $K_s$ , and  $G$ , as indicated in the top left corner of each plot. The input magnitudes are reddened according to the extinction  $A_V$  labelled within each plot.

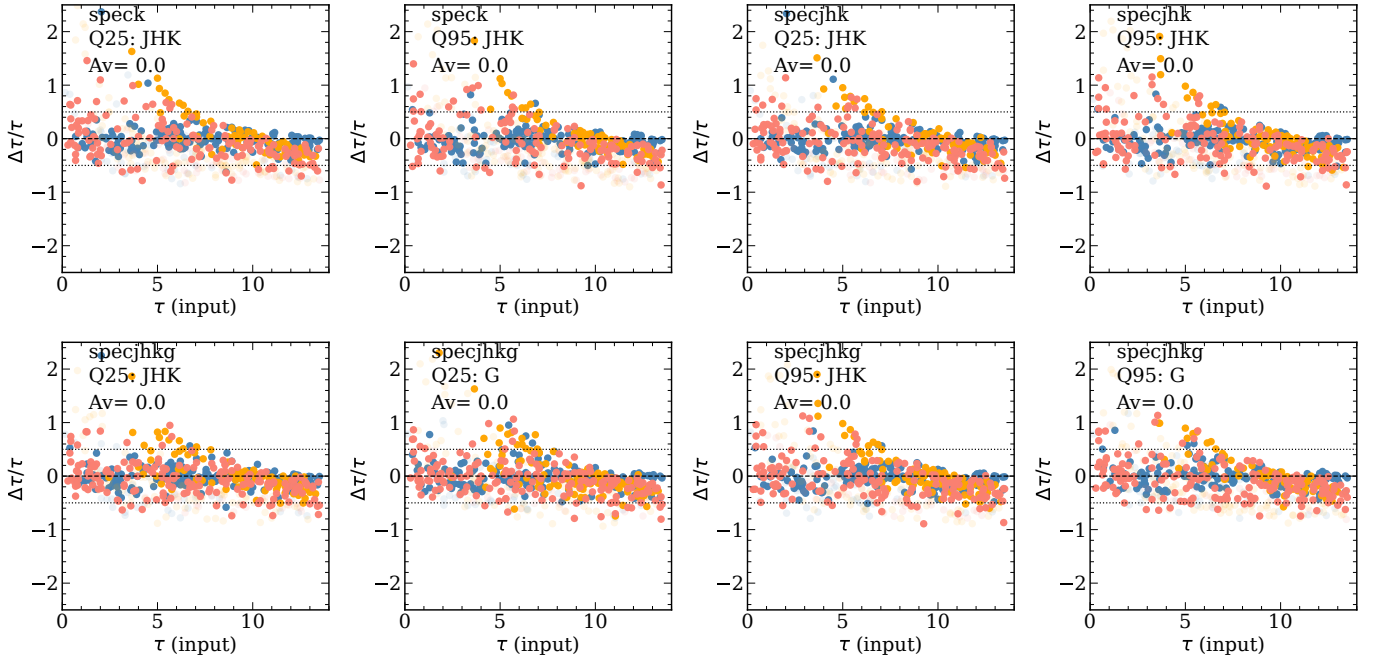


**Fig. B.1.** Comparison of the input ages vs the relative error of the output ones, for the speck, specjnhk, and specjnhkg projections, with Q50 uncertainties in  $T_{\text{eff}}$ ,  $\log g$ , and  $[M/H]$ , and uncertainties in  $J$ ,  $H$ ,  $K_s$ , and  $G$  as indicated in the top left corner of each plot. No interstellar extinction is considered here.

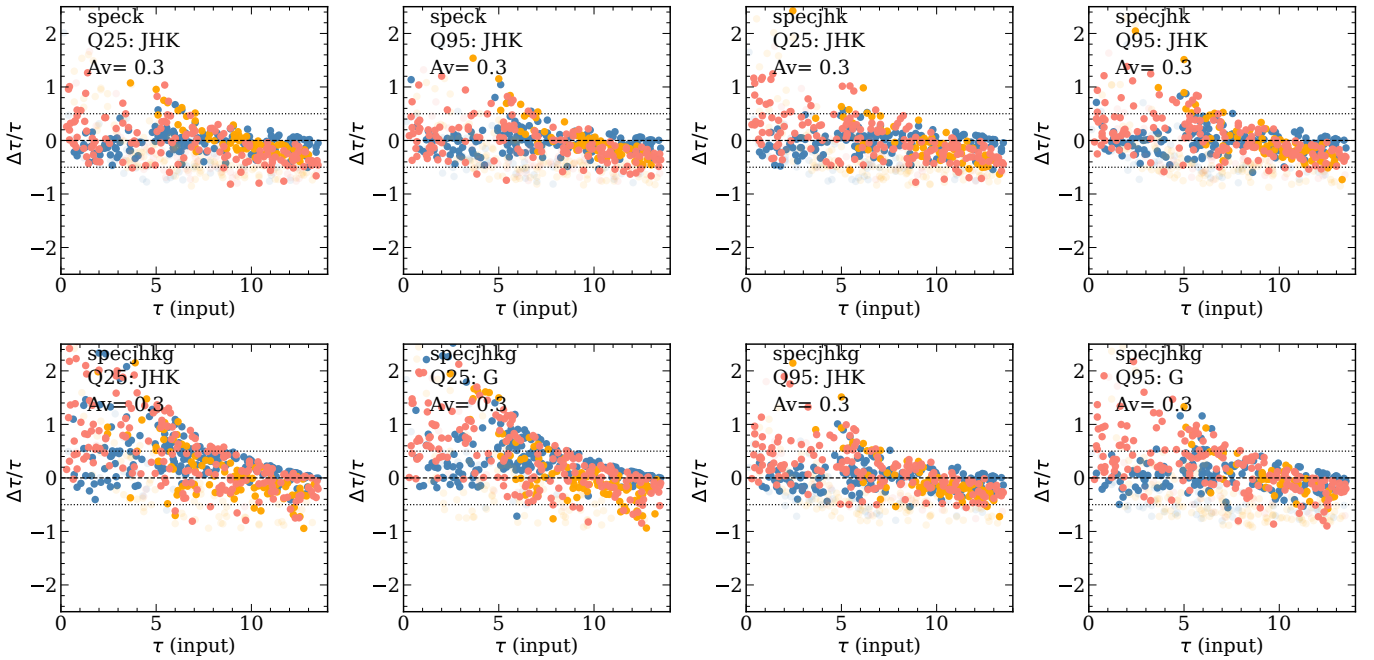


**Fig. B.2.** Similar to Fig. B.1, but with an extinction of  $A_V = 0.3$  mag.

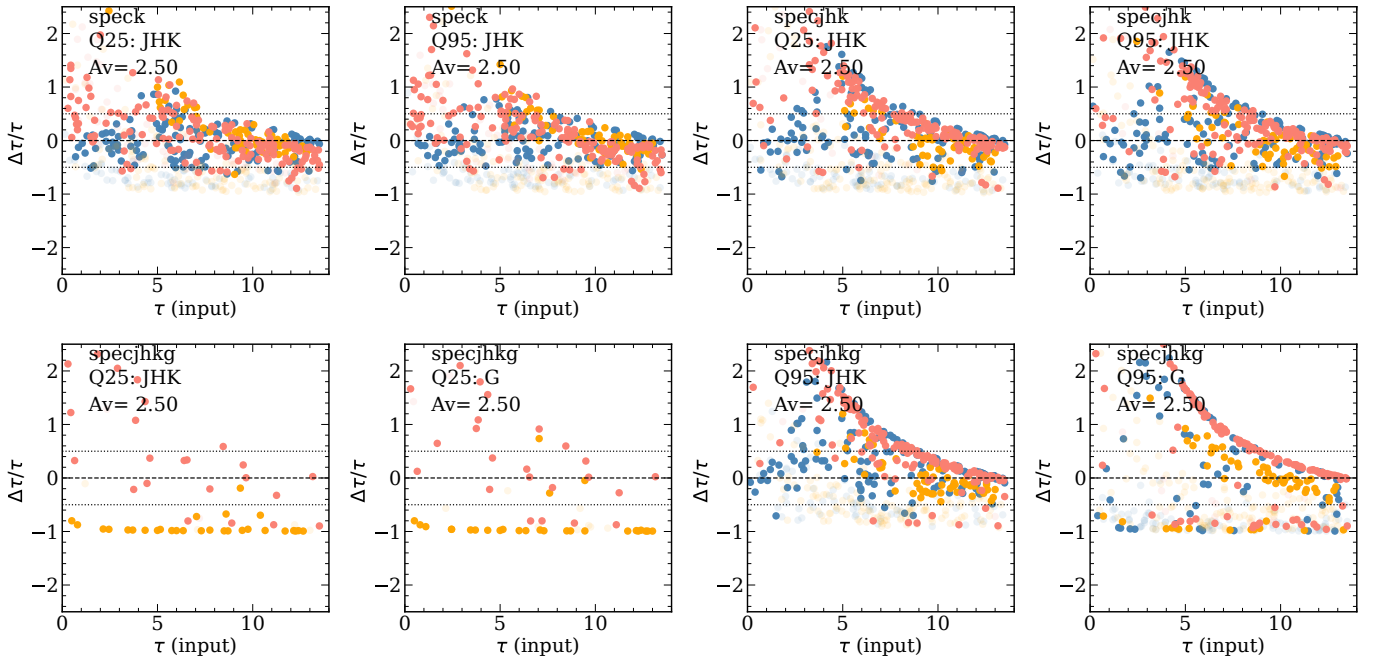


**Fig. B.3.** Similar to Fig. B.1, but with an extinction of  $A_V = 2.5$  mag.

## Appendix C: Open and globular cluster plots

Figures C.1 and C.2 show open and globular cluster targets, in the  $T_{\text{eff}}\text{-}\log g$  and  $T_{\text{eff}}\text{-}M_{K_s}$  spaces. In red are plotted the

isochrones with metallicity and age equal to the mean GSP-Spec (calibrated) metallicity and mean derived age of the cluster stars, whereas in black we plot the isochrones for the reference age.

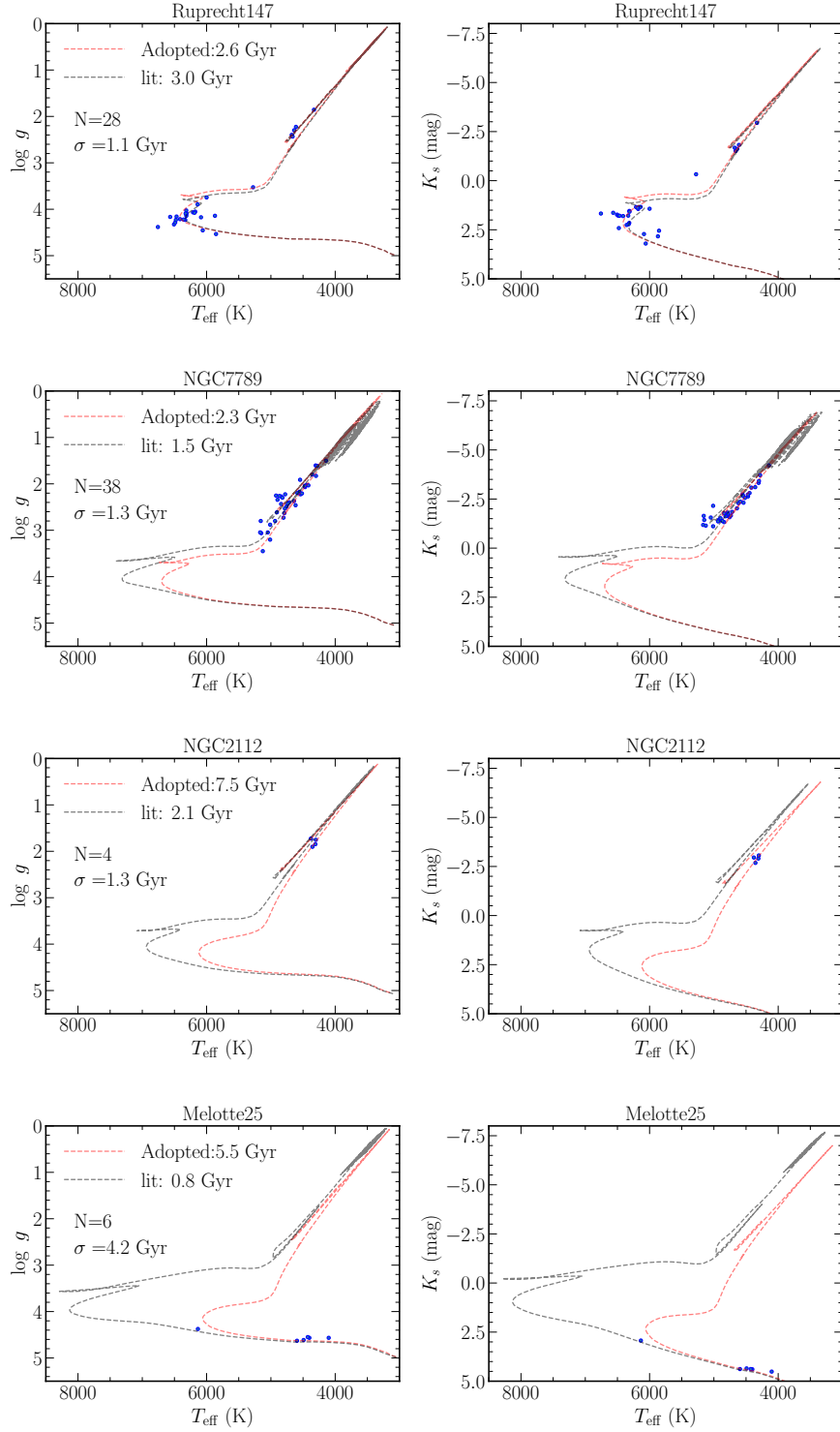


**Fig. C.1.**  $T_{\text{eff}}\text{-}\log g$  (left) and  $T_{\text{eff}}\text{-}M_{K_s}$  (right) diagrams for a few cherry-picked open clusters. The isochrones of the adopted mean age (in red) and the reference age from [Cantat-Gaudin et al. \(2020\)](#) are plotted in red and black, respectively, for the mean metallicity of the cluster derived from the calibrated GSP-Spec values. The first two rows show examples for which our ages and the literature values are in good agreement. The bottom two rows show the opposite: for NGC2112 our solution fits the data better than the younger isochrone, pointing towards offsets in the input  $T_{\text{eff}}$ ,  $[M/H]$ , or distance modulus. For NGC7789, our solution is not reliable, since main-sequence stars do not constrain the ages well enough.

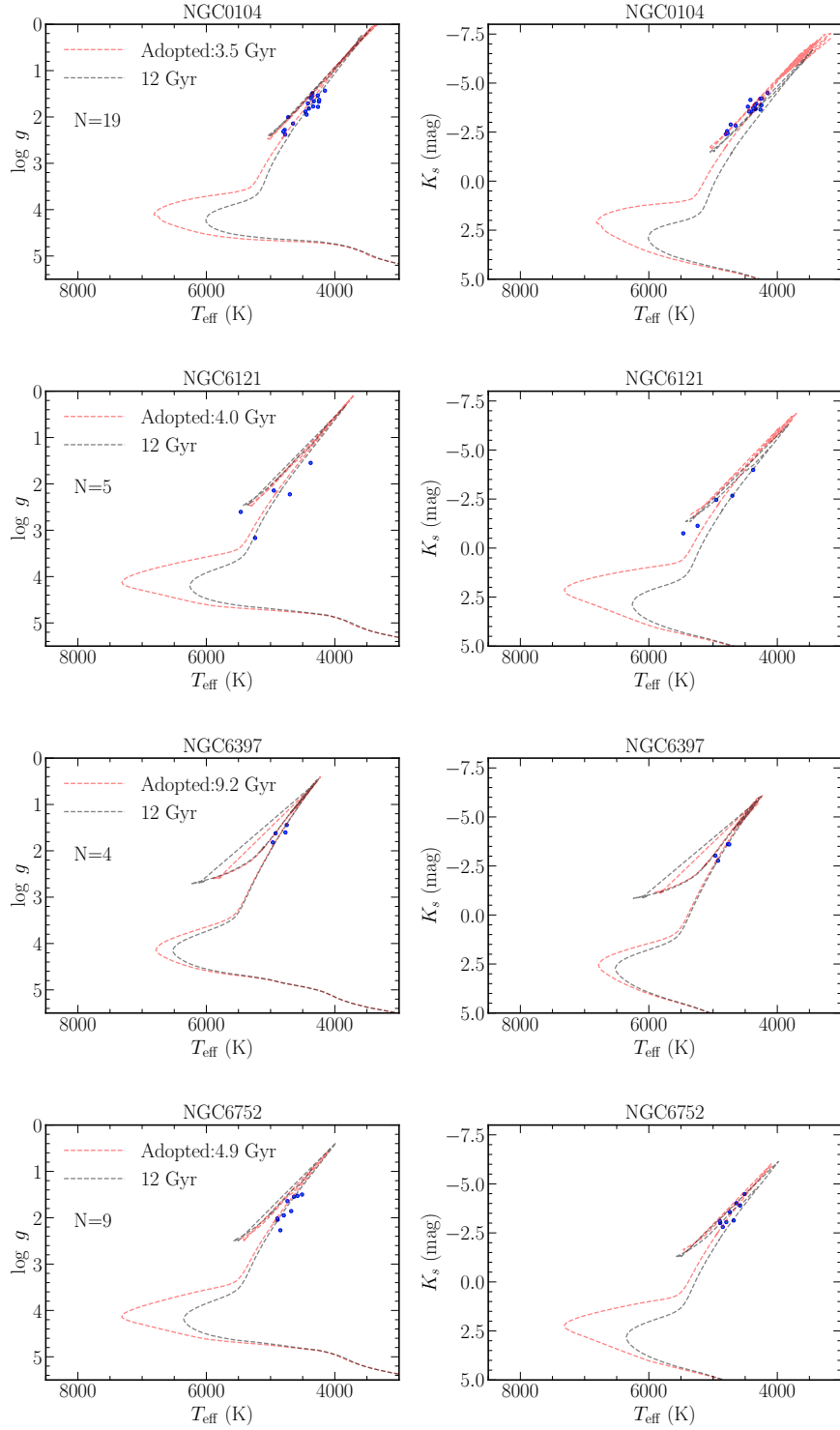


**Fig. C.2.**  $T_{\text{eff}}$ - $\log g$  (left) and  $T_{\text{eff}}$ - $M_{K_s}$  (right) diagrams for a few cherry-picked globular clusters. Candidate stars were selected based on the results of [Gaia Collaboration \(2018c\)](#). The isochrones with the adopted mean age (in red) and for 12 Gyr are plotted in red and black, respectively, for the mean metallicity of the cluster derived from the calibrated GSP-Spec values.